

In-plane uniaxial magnetic anisotropy induced by anisotropic strain relaxation in high lattice-mismatched Dy/Sc superlattices

L. Benito,^{1,2,*} C. Ballesteros,³ and R. C. C. Ward⁴¹*Departamento de Física de la Materia Condensada, Universidad de Zaragoza, 50009 Zaragoza, Spain*²*Cavendish Laboratory, J. J. Thomson Avenue, University of Cambridge, Cambridge, CB3 0HE, United Kingdom*³*Departamento de Física, Universidad Carlos III, 28911 Leganés, Madrid, Spain*⁴*Oxford Physics, Clarendon Laboratory, Parks Road, University of Oxford, Oxford OX1 3PU, United Kingdom*

(Received 25 November 2013; revised manuscript received 17 February 2014; published 23 April 2014)

We report on the magnetic and structural characterization of high lattice-mismatched [Dy_{2nm}/Sc_{t_{sc}}] superlattices, with variable Sc thickness $t_{sc} = 2\text{--}6$ nm. We find that the characteristic in-plane effective hexagonal magnetic anisotropy $K_6^{6,ef}$ reverses sign and undergoes a dramatic reduction, attaining values of $\approx 13\text{--}24$ kJm⁻³, when compared to $K_6^6 = -0.76$ MJm⁻³ in bulk Dy. As a result, the basal plane magnetic anisotropy is dominated by a uniaxial magnetic anisotropy (UMA) unfound in bulk Dy, which amounts to $\approx 175\text{--}142$ kJm⁻³. We attribute the large downsizing in $K_6^{6,ef}$ to the compression epitaxial strain, which generates a competing sixfold magnetoelastic (MEL) contribution to the magnetocrystalline (strain-free) magnetic anisotropy. Our study proves that the in-plane UMA is caused by the coupling between a giant symmetry-breaking MEL constant $M_{\gamma,2}^2 \approx 1$ GPa and a morphic orthorhombiclike strain $\varepsilon_{\gamma,1} \approx 10^{-4}$, whose origin resides on the arising of an in-plane anisotropic strain relaxation process of the pseudoepitaxial registry between the nonmagnetic bottom layers in the superstructure. This investigation shows a broader perspective on the crucial role played by epitaxial strains at engineering the magnetic anisotropy in multilayers.

DOI: [10.1103/PhysRevB.89.134421](https://doi.org/10.1103/PhysRevB.89.134421)

PACS number(s): 75.30.Gw, 75.50.Cc, 75.70.Cn

I. INTRODUCTION

Thin films and multilayers [1,2] (MLs) are usually subject to epitaxial stress due to the lattice misfit and clamping effects caused by the combined action of buffer layers and substrate. The arising of epitaxial strains in low-dimensional systems is the origin for large magnetoelastic (MEL) contributions, through the inverse MEL coupling [3], to the magnetic anisotropy [4] energy (MAE), which in turn determines the magnetic moment orientation [5], coercivity, and magnetic domain-wall [6] dynamics. Undoubtedly, the ultimate outcome is a MEL-induced switching [7,8] of the easy direction. Gaining a better understanding on the manner in which the strained state of multilayered nanostructure modifies the magnetic anisotropy and, therefore, its magnetic response, is instrumental in ensuring the correct performance of spin-based nanodevices [9].

For nonisotropic thin-film layers, the appearance of epitaxial strains inevitably leads to an anisotropic strain state, if one compares in-plane and out-of-plane strain. Moreover, the same argument is valid for the deposition plane, wherein under certain circumstances the in-plane lattice parameter can become slightly anisotropic. Thus, the lattice symmetry-breaking effect that takes place at the interface during the deposition of magnetic heterostructures possessing dissimilar crystal-lattice structures triggers an anisotropic strain relaxation [10] (ASR) of the lattice parameter, which may induce changes in the magnetic properties. Not surprisingly, in *ultrathin* 3d ferromagnetic layers, the emergence of such anisotropic lattice distortion gives rise to an in-plane uniaxial magnetic anisotropy (UMA), as shown in cubic 3d/semiconductor [11,12] hybrid nanostructures, Co/W [13,14] and Co/Mo [15]

bilayers. Even for thicker layers, the lithography process applied to pattern the magnetic media [16,17] induces an ASR in the overlayer, which in turn gives rise to an easy-axis spin reorientation.

The deposition techniques pioneered by Kwo *et al.* [18] established a procedure to synthesize high-quality RE-based heterostructures [19], which allowed us to probe fundamental concepts in rare-earth (RE) magnetism [20,21]. The synthesis of a high-quality single-crystal RE thin film is typically achieved by depositing RE metals onto a (110) template surface of a bcc transition metal, that is, V [22], Nb [18], Mo [23], and W [24,25]. These techniques [18] entail the pseudocoherent registry of dissimilar (0001) hexagonal-closed-packed (hcp) and (110) body-centered-cubic (bcc) surfaces, which triggers an ASR at the interface [26,27]. This fact can potentially induce an in-plane anisotropic lattice distortion in the on-top deposited RE-based thin film or multilayer, unless the in-plane lattice parameter of the seed layer, typically a nonmagnetic hexagonal metal such as Y, Lu, Sc, or Zr, is isotropically relaxed. A recent study by Saraf *et al.* [28] has shown that, in the case an ASR mechanism occurs, the in-plane lattice parameter anisotropy not only persists at the top surface in the deposited layer, but is further enhanced as this latter grows thicker.

The likely emergence of a symmetry-breaking ASR process in RE-based multilayered heterostructures raises the intriguing possibility of generating huge low-symmetry MEL contributions to MAE, which potentially can lead to large modifications in their magnetic properties, given that RE metals possess a giant MEL coupling [29,30]. Surprisingly, despite that Kwo *et al.* [18] deposition techniques are regarded as a standard in thin-film technology, there exists a poor understanding on the repercussions that the ASR process has upon the magnetic anisotropy in RE-based multilayered nanostructures.

In this paper, unlike prior studies [11–17], we have conducted a structural characterization, by means of

*luisbenito.phys@gmail.com

high-resolution x-ray diffraction (HRXRD) and transmission electron microscopy (HRTEM), and investigated the magnetic properties, mainly, magnetization, magnetic anisotropy (obtained from magnetic torque curves), and magnetostriction, with the aim to correlate changes in the magnetic response to modifications in the lattice microstructure in highly lattice-mismatched Dy/Sc *multilayered* nanostructure. Our study reveals that the in-plane sixfold effective magnetic anisotropy $K_6^{6,ef}$ has reversed sign and dramatically diminished when compared to that in bulk Dy. Furthermore, the easy-plane anisotropy is dominated by the emergence of a uniaxial magnetic anisotropy (UMA). We develop arguments that prove that the downsizing of the sixfold anisotropy constant is caused by a large epitaxial compression strain and the in-plane UMA is originated in an *anisotropic strain relaxation* process at the Nb/Sc interface, which gives rise to an anisotropic in-plane lattice parameter in the Sc layer, so that such a lattice anisotropy is transferred into the Dy/Sc multilayer. Beyond the particular interest for RE-based thin-film magnetism, our work provides an unprecedented perspective on the potential impact that epitaxial strains have upon the magnetic anisotropy in complex multilayered nanostructures.

II. EXPERIMENTAL METHODS

A. Growth of Dy/Sc SLs

We have investigated a set of *c*-grown $[\text{Dy}_{t_{\text{Dy}}}/\text{Sc}_{t_{\text{Sc}}}]_{50}$ superlattices (SLs), where the nominal Dy and Sc layer thickness are $t_{\text{Dy}} = 20$ Å and $t_{\text{Sc}} = 20, 30, 40,$ and 60 Å, respectively, and 50 refers to the number of bilayer, Dy/Sc, repetitions. The SLs were grown by means of a molecular beam epitaxy technique in an ultrahigh vacuum chamber (Balzers UMS630) with a base pressure better than 2×10^{-10} mbar. A detailed description of the deposition techniques used can be found elsewhere [31,32]. Briefly, an initial Nb buffer layer 50 nm thick is deposited onto a heated “epi-polished” (11 $\bar{2}$ 0)-oriented ($\pm 1^\circ$) Al_2O_3 substrate typically 1 mm thick, and, after that, a Sc seed layer 120 nm thick is grown. The deposition conditions for the $[\text{Dy}_{20}/\text{Sc}_{t_{\text{Sc}}}]_{50}$ SL are chosen to allow the multilayer to accommodate the large lattice mismatch (-7.9%) between Dy and Sc layers [33]. These deposition techniques [31,32] assure the epitaxial relationships at the (110)_{Nb} \parallel (1120)_{Al₂O₃} are such that the threefold axes in the two lattice structures are aligned [33,34], i.e., $[1\bar{1}1]_{\text{Nb}} \parallel [0001]_{\text{Al}_2\text{O}_3}$ and $[1\bar{1}2]_{\text{Nb}} \parallel [1\bar{1}00]_{\text{Al}_2\text{O}_3}$, and the relationship for the crystalline planes is $\{1120\}_{\text{Al}_2\text{O}_3} \parallel \{110\}_{\text{Nb}} \parallel \{0001\}_{\text{Sc}} \parallel \{0001\}_{\text{Dy/Sc}}$.

B. Magnetometry: Magnetic torque curves

Magnetic torque experiments were performed in a *home-made* high-resolution vector vibrating sample magnetometer (VVSM) [35]. The sample is rotated with respect to the applied magnetic field \mathbf{H} so that the rotation axis is collinear to the hexagonal axis of the sample, whereas \mathbf{H} is applied in the basal plane (BP) of the hcp structure, as shown in Fig. 1(a). The VVSM yields the longitudinal $M_{\parallel}(\varphi)$ and transversal $M_{\perp}(\varphi)$ components of the total magnetization \mathbf{M} with respect to \mathbf{H} in the rotation plane, as a function of the rotation angle φ [see Fig. 1(b)]. \mathbf{M} and \mathbf{H} make angles ϕ and φ , respectively, with the

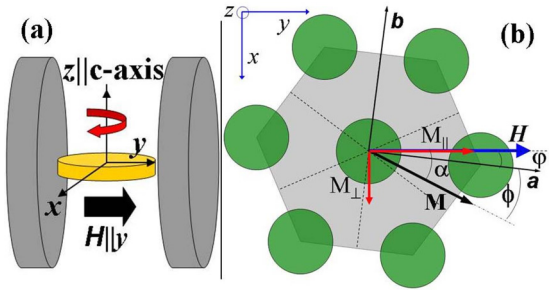


FIG. 1. (Color online) Sketch of sample's rotation. (a) The magnetic field \mathbf{H} is applied in the *c* plane, so that \mathbf{c} is the rotation axis and the Cartesian (x, y, z) axes are taken such as $z \parallel \mathbf{c}$ and, at the beginning of the torque experiment, $x \parallel \mathbf{b}$ and $y \parallel \mathbf{a}$. (b) The longitudinal M_{\parallel} and transversal M_{\perp} components of the total magnetization \mathbf{M} with respect to \mathbf{H} in the rotation plane. Assuming the easy direction for \mathbf{M} is the \mathbf{a} direction, this makes an angle φ with \mathbf{H} , and \mathbf{M} makes angles α and ϕ (crystal angle) with \mathbf{H} and the \mathbf{a} direction, respectively. See text for further details.

easy direction in the sample, and α is the angle that makes \mathbf{M} with \mathbf{H} . At equilibrium, the magnetic torque $L_k(\phi)$ is obtained by minimizing the total energy $E_T = E_Z + E_A$ where E_Z is the Zeeman energy and E_A is the effective anisotropy energy. Demagnetization energy is neglected in our case because the demagnetizing factor $N_D = 0$ since \mathbf{H} is applied in plane. Thus, L_k can be obtained from $M_{\perp}(\varphi)$ as follows:

$$L_k(\phi) = -\partial E_A / \partial \phi = -BM \sin \alpha = -HM_{\perp}(\varphi). \quad (1)$$

We directly determine $M_{\perp}(\varphi)$ and we gain access to $M_{\parallel}(\varphi)$ by using the relationship $\phi = \alpha - \varphi$, where α is also experimentally determined as $\alpha(\varphi) = \arctan[M_{\perp}(\varphi)/M_{\parallel}(\varphi)]$.

High-field magnetization and magnetoelastic measurements are carried out in a VSM12[©] high-field facility. M - H loops are collected by applying \mathbf{H} along the easy axis for \mathbf{M} in the Dy/Sc SLs, unless otherwise stated. M - H loops are properly corrected against diamagnetic and paramagnetic contributions from substrate and Sc buffer layer. Zero-field-cooled (ZFC) and field-cooled (FC) M - T curves are collected in a SQUID magnetometer (Quantum Design).

C. Cantilever technique and MEL constant $M_{y,2}^2$

The MEL stresses are determined by using a capacitive cantilever technique [36–38], where the bending of a cantilever, a bimorph made of the sapphire substrate plus the Dy/Sc SL, can be detected as capacitance change in a capacitive apparatus. The capacitive cell is made of machinable glass ceramic (Macor[©]) [39], which assures a good thermal stability (see sketch in Fig. 2). The capacitive probe fits in a constant-flow cryostat, which is fitted in a VSM12[©] facility, so that temperature can be varied from 4.2 up to 300 K and the H range is ± 12 T. The capacitive cell can be rotated 90° and so \mathbf{H} can be applied along or transversal to the clamping edge.

Obtaining a relationship between the deflection at the end of the cantilever Δ and the MEL stress σ needs of the zero transversal curvature approximation to determine Δ , derived from the manner in which the bending of the cantilever transversal to its width from the clamping line is considered.

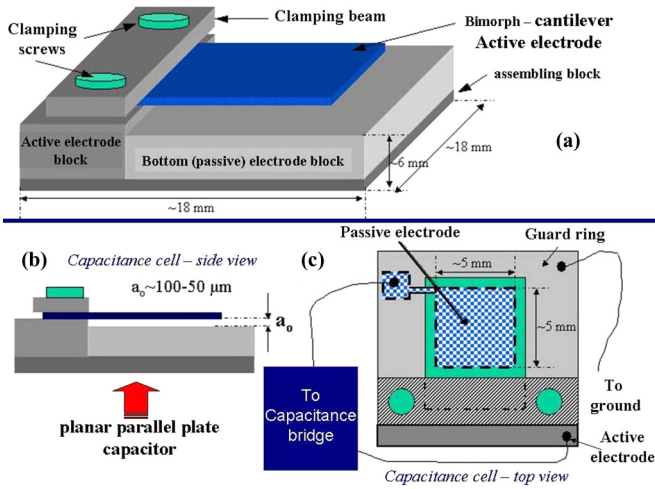


FIG. 2. (Color online) (a) Overall view of the capacitive cell fabricated in machinable glass ceramic (Macor). (b) Side view of the capacitive cell, which shows the customized gap between the passive-fixed electrode and the active-cantilever one a_0 . (c) Top view of the capacitive cell, which shows the active electrode (cantilever) covering the full area of the passive electrode. Briefly, a two-side polished (Macor[®]) plate is cut into two pieces, where the smallest one, active block (B1), is used as support to clamp and hold the cantilever (sample) using a clamping beam. The largest, passive block (B2) is further thinned down, so that a_0 can be customized, typically $a_0 \sim 100 \mu\text{m}$ in our capacitive cell. B1 and B2 are coated by a sputtered Al $\sim 200\text{-nm}$ -thick layer. The cantilever is placed face down and in electrical contact with B1; once clamped, the cantilever completely covers the sensing area, which guarantees a constant capacitance $\approx 2.25 \text{ pF}$ at room temperature.

Watts *et al.* [40] showed that the deflection ratio between the zero transversal curvature Δ_{flat} and the free bending curvature Δ_{free} is $\Delta_{\text{flat}}/\Delta_{\text{free}} = 1 - \nu$, where ν is the Poisson's ratio for the a -plane-oriented sapphire substrate [41]. In this case, for $\text{Al}_2\text{O}_3[\bar{1}2\bar{1}0]$, we calculate that $\nu = 0.0805$ [42–44] and, thus, $\Delta_{\text{flat}}/\Delta_{\text{free}} \approx 1$. In this way, Δ can be obtained from a modified Stoney's formula [45]

$$\sigma = \frac{1}{3} \frac{Y}{1 - \nu^2} \frac{t_s^2}{t_{\text{SL}} L^2} \Delta_{\text{flat}}, \quad (2)$$

where Y is the Young's modulus of the substrate, t_s and t_{SL} are the substrate's and superlattice thickness, respectively, and L is the cantilever length at the end of which Δ_{flat} is determined. Now, for small deflections, that is, $\Delta/a_0 \ll 1$ where a_0 is the gap between electrodes in the capacitive cell, and assuming zero transversal curvature deflection for the cantilever, Δ can then be determined by means of a capacitive technique, where the capacitance change ΔC is related to Δ_{flat} as follows: $\Delta C = (\frac{2}{3} \frac{C_o^2}{A \epsilon_0}) \Pi \Delta_{\text{flat}}$ where C_o is the zero-field capacitance value, ϵ_0 is the vacuum permittivity, A is the fixed electrode capacitor area, and Π is a geometrical factor, which depends on the relative distances between the cantilever clamping line and the edge of the fixed electrode. ΔC can be measured with high accuracy ($\approx 10^{-6} \text{ pF}$) using an Andeen-Hagerling capacitive bridge [46]. From the above, it is then straightforward to calculate that the smallest measurable Δ_{flat} corresponds to $\approx 2 \text{ \AA}$. We notice that the sapphire substrate is carefully thinned

down to typically $200\text{--}400 \mu\text{m}$ in order to reduce the clamping effect and thus to increase the sensitivity of the cantilever technique, given that $\Delta_{\text{flat}} \propto 1/t_s^2$ as seen in Eq. (2). Further to the validity of Eq. (2), a finite element analysis of the bending of crystalline plates carried out by Dahmen *et al.* [47] predicts that the bending becomes nonuniform as a result of the constraints imposed by the clamping, so that Eq. (2) is subject to uncertainty, leading to some error at obtaining σ from the bending of the bimorph. Experimentally, Ciria *et al.* [48] tested the accuracy of the cantilever technique, showing that the measured average $M_{\gamma 2}$ for Ho thin films 0.5 and $1.0 \mu\text{m}$ thick yielded 0.29 and 0.28 GPa , respectively, in good accord with the bulk value 0.275 GPa [49]. Based on this, we conclude that the error associated to assuming a uniform bending/curvature in Eq. (2) has little influence on the determination of the MEL constant.

For RE-based heterostructures, Ciria *et al.* [50] found a relationship which relates *magnetostriction*, magnetoelastic stress, and deflexion (curvature) for an anisotropic cantilever. Extending the above study [50] by considering MEL constants up to rank $l=4$ in the MEL energy, then finding $\sigma[\alpha, \beta]$ for the high-symmetry directions in hexagonal symmetry, so that $\{\alpha, \beta\} = \{a, b\}$, leads to a set of four independent relationships, which relate $\sigma[\alpha, \beta]$ to a combination of MEL constants, so that $\sigma[\alpha, \beta]$ stands for a MEL stress obtained when $\mathbf{H} \parallel \alpha$ and the deflexion of the cantilever is measured along the β direction. These relationships read [51] as

$$\sigma[a, a] = \chi \frac{C_{xx}}{R_x} = -\frac{1}{4} \left(M_{\gamma, 2}^2 - \frac{1}{3} M_{\gamma, 2}^4 \right) - \frac{1}{4} M_{\gamma, 4}^4 - \Omega, \quad (3)$$

$$\sigma[a, b] = \chi \frac{C_{yy}}{R_y} = \frac{1}{4} \left(M_{\gamma, 2}^2 + \frac{1}{3} M_{\gamma, 2}^4 \right) + \frac{1}{4} M_{\gamma, 4}^4 - \Omega, \quad (4)$$

$$\sigma[b, a] = \chi \frac{C_{xx}}{R_x} = \frac{1}{4} \left(M_{\gamma, 2}^2 - \frac{1}{3} M_{\gamma, 2}^4 \right) - \frac{1}{4} M_{\gamma, 4}^4 - \Omega, \quad (5)$$

$$\sigma[b, b] = \chi \frac{C_{yy}}{R_y} = -\frac{1}{4} \left(M_{\gamma, 2}^2 - \frac{1}{3} M_{\gamma, 2}^4 \right) + \frac{1}{4} M_{\gamma, 4}^4 - \Omega, \quad (6)$$

where $\chi = \frac{1}{6} \frac{t_s^2}{t_{\text{SL}}}$, $C_{xx} = 477.8 \text{ GPa}$, and $C_{yy} = 447.8 \text{ GPa}$ result from a combination of elastic constants for sapphire [52], R_x^{-1} and R_y^{-1} are the cantilever curvatures along the Cartesian x and y axes, respectively, and are experimentally obtained as [50] $R_i^{-1} = -6\epsilon_0 A \Delta C_i / L_i^2 C_{i0}^2$, Ω stands for a complex combination of elastic and isotropic MEL constants, and $M_{\gamma, l}^m$ are MEL constants associated to the symmetric γ strictions $\epsilon_{\gamma 1}$ and $\epsilon_{\gamma 2}$ in hexagonal symmetry. We have opted for *del Moral's* notation [53], where MEL constants are now referred as $M_{\Gamma, n}^l \equiv B_{\Gamma, n}^l$, where $B_{\Gamma, n}^l$ are MEL constants according to Callen's notation [54]. An earlier revision [29] of Dy magnetostriction found that $M_{\gamma 4}^4 \approx 0$ and the ratio $M_{\gamma 2}^4 M_{\gamma 2}^2 \approx 0.25$. Inserting these two latter expressions in

(3)–(6) leads to the following relationships:

$$\begin{aligned}\sigma[a,a] &= \sigma[b,b], \\ \sigma[a,b] &= \sigma[b,a].\end{aligned}\quad (7)$$

Building on the exceptional performance of our capacitive cell, which assures a highly stable and reproducible measurements, we have been able to test that the relationships in Eq. (7) remain valid in the Dy/Sc SLs, within the experimental error ($\pm 2\%$). Therefore, making use of Eq. (7), $M_{\gamma_2}^2$ is unambiguously determined by the relationship

$$2(\sigma[b,a] - \sigma[a,a]) = \chi \left\{ \left. \frac{C_{xx}}{R_x} \right|_{\mathbf{H}\parallel\mathbf{b}} - \left. \frac{C_{xx}}{R_x} \right|_{\mathbf{H}\parallel\mathbf{a}} \right\} \equiv M_{\gamma_2}^2, \quad (8)$$

where $M_{\gamma_2}^2$ is obtained by performing two MEL measurements, that is, by clamping the cantilever along the \mathbf{b} direction and by determining $\sigma[b,a]$, whereas $\mathbf{H} \perp \mathbf{a}$, and $\sigma[a,a]$ where $\mathbf{H} \parallel \mathbf{a}$, where the \mathbf{a} direction is the easy direction for M in bulk Dy. Experimentally, this is achieved by rotating 90° the capacitive cell in the capacitive probe, whereas the cantilever is kept clamped along \mathbf{b} and \mathbf{H} is collinear to the axis probe. Finally, in Eq. (8), C_{xx} is considered temperature independent [42–44] and the room temperature value is typically used.

D. Transmission electron microscopy and x-ray diffraction techniques

The morphology and structure of the Dy/Sc SLs have been studied by transmission electron microscopy (TEM) in a Philips Tecnai 20F FEG analytical microscope operating at 200 keV. The x-ray diffraction (XRD) measurements were carried out using a triple-crystal Philips MRD high-resolution x-ray diffractometer with an incident wavelength of 1.54056 \AA from a Cu K_α x-ray radiation source and a multiple bounce Ge(111) monochromator and analyzer. The scattering wave vector \mathbf{Q} was varied parallel and perpendicular to the (0001) layer surface through the center of the Bragg peaks of the scandium seed layer. These scans were defined by two components: $Q_z \parallel [0001]$ and $Q_x \parallel [10\bar{1}0]$. Scans in which Q_x were varied are referred to as transverse scans, while those in which Q_z varied are referred to as longitudinal on axis. \mathbf{Q} resolution in the scattering plane and transverse to the scattering vector is typically better than $\sim 4 \times 10^{-4}$ and $\sim 3 \times 10^{-2} \text{ \AA}^{-1}$, respectively.

III. RESULTS AND ANALYSIS

A. Superlattices structural characterization: Transmission electron microscopy and x-ray diffraction

The metallic species Dy and Sc crystallize in the hexagonal-close-packed (hcp) lattice structure [55] and their lattice parameters are $a_{\text{Dy}} = 3.593 \text{ \AA}$ and $c_{\text{Dy}} = 5.655 \text{ \AA}$, and $a_{\text{Sc}} = 3.309 \text{ \AA}$ and $c_{\text{Sc}} = 5.268 \text{ \AA}$, respectively. From these, we calculate that the lattice misfit between the Dy and Sc in-plane lattice parameters is $\varepsilon_0 = (a_{\text{Sc}} - a_{\text{Dy}})/a_{\text{Dy}} = -0.079$.

Structural characterization is illustrated by presenting data collected in the $(\text{Dy}_{20}/\text{Sc}_{60})_{50}$ SL, which shows in an exemplary manner the results obtained in the series. Figure 3(a)

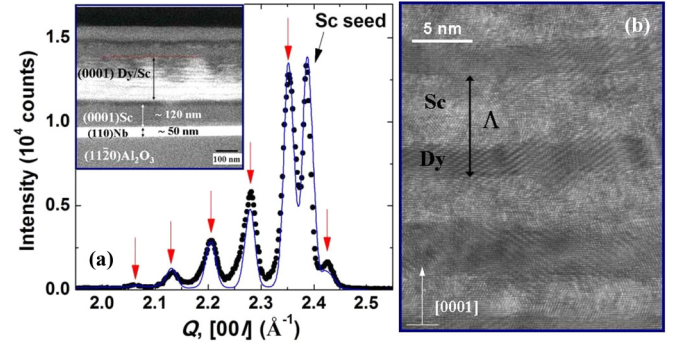


FIG. 3. (Color online) (a) X-ray diffraction intensity for a longitudinal scan of the scattering wave vector \mathbf{Q} along the direction [001]. Red arrows mark the superlattice reflections and the black arrow the Sc seed layer one. The line is a fit according to the model developed by Jehan *et al.* [56]. The best-fit parameters are displayed in Table I. Inset shows a cross-sectional HAADF-STEM image of $(11\bar{2}0)\text{Al}_2\text{O}_3/(110)\text{Nb}/(0001)\text{Sc}/[\text{Dy}_{22.2\text{ \AA}}/\text{Sc}_{63.3\text{ \AA}}]_{50}$ SL. (b) HRTEM image of the Dy/Sc multilayer structure close to the Sc seed layer. Dark and light contrast represent Dy and Sc layers, respectively.

displays a typical longitudinal high-resolution x-ray diffraction (HRXRD) scan showing superlattice order, where only the lowest- Q reflections corresponding to the multilayer structure peaks and those for the Sc seed layer are displayed. HRXRD longitudinal scans around the (0002) Bragg reflection have been fitted for all four Dy/Sc SLs using the model developed by Jehan *et al.* [56], and a summary of the best-fit parameters is displayed in Table I. As a brief note, we find that interface roughness and structural coherence along growth direction yield comparable values to those obtained previously in Ho/Sc [33] SLs. We also observe that the c lattice parameter of the Sc seed layer $c_{\text{Sc}}^{\text{seed}}$ is almost relaxed to the bulk value. Thus, we estimate that $c_{\text{Sc}}^{\text{seed}} = 5.2685 \pm 0.0004 \text{ \AA}$. The lower resolution of transversal scans around the Bragg (1004) reflection prevents resolving a differentiated in-plane parameter for all four SLs. From the transversal scans, we calculate that the in-plane lattice parameter for the Dy and Sc layers in the SLs and the structural coherent length ξ are

TABLE I. Parameters obtained from fitting XRD longitudinal scans in $(\text{Dy}_{t_{\text{Dy}}}/\text{Sc}_{t_{\text{Sc}}})_{50}$ SLs using the Jehan *et al.* [56] model. t_{Dy} and t_{Sc} are nominal thickness for the Dy and Sc layers and t_{Dy}^* and t_{Sc}^* correspond to the fitted values, d_{Dy} and d_{Sc} are the interatomic spacing for Dy and Sc layers along the c axis, σ is the interatomic diffusion or roughness at the Dy-Sc interfaces, in atomic monolayers (MLs), and ξ is the spatial coherence along the c axis, calculated as $\xi = 2\pi/\Delta Q$, where ΔQ is the full width at half maximum (FWHM) at the main Dy/Sc superlattice reflection. All parameters are given in \AA , except σ , which is given in atomic layers (ALs).

| $t_{\text{Dy}}/t_{\text{Sc}}$ | $t_{\text{Dy}}^*/t_{\text{Sc}}^*$ | d_{Dy} | d_{Sc} | $\sigma(\pm 1 \text{ AL})$ | $\xi(\pm 50 \text{ \AA})$ |
|-------------------------------|-----------------------------------|-----------------|-----------------|----------------------------|---------------------------|
| 20/60 | 22.2/63.3 | 2.901 | 2.6335 | 2 | 480 |
| 20/40 | 21.5/41.2 | 2.886 | 2.6324 | 2 | 510 |
| 20/30 | 21.2/29.0 | 2.873 | 2.6316 | 2 | 560 |
| 20/20 | 22.6/22.3 | 2.846 | 2.6299 | 1 | 590 |

$a_{\text{Dy}}^{\text{SL}} = 3.51 \pm 0.03 \text{ \AA}$ and $a_{\text{Sc}}^{\text{SL}} = 3.30 \pm 0.03 \text{ \AA}$, and $\xi_{\text{Dy}} \approx 10 \text{ \AA}$ and $\xi_{\text{Sc}} \approx 25 \text{ \AA}$, respectively. Similarly, prior XRD studies conducted in Ho/Sc [33] SL found a clearly differentiated a lattice parameter for Ho and Sc layers, and Sc seed layer. For instance, for the $(\text{Dy}_{20}/\text{Sc}_{60})_{50}$ SL, we calculate that for the Dy layers, the average in-plane strain is $\varepsilon_{\parallel} = -0.0231$ and the out-of-plane strain is $\varepsilon_{\perp} = 0.0256$. Notice that, as found in other systems [57], $\varepsilon_{\perp} > |\varepsilon_{\parallel}|$ in opposition to the Poisson's ratio [58], i.e., $\varepsilon_{\perp} = -2\varepsilon_{\parallel} \frac{c_{13}}{c_{33}}$, where c_{13}/c_{33} ($=0.263$ [59]) is taken as the bulk value. Apparently, the origin of the anomalous strains in multilayered systems seems to be related to the electronic band mismatching [60] (dissimilar Fermi energy and/or electronic band structure) between constituents and, therefore, it is difficult to accurately separate out from the epitaxial strains. For simplicity, we will proceed with our analysis assuming strains are primarily epitaxy driven and, for the sake of accuracy, we will work out equations around ε_{\perp} .

The inset graph in Fig. 3(a) shows a cross-sectional high-angle annular dark-field scanning transmission electron microscopy (HAADF-STEM) image, where Nb buffer and Sc seed layers are seen at the bottom and the Dy/Sc multilayered heterostructure at the top. From the high-resolution transmission electron microscopy (HRTEM) image, shown in Fig. 3(b), we estimate that the Dy/Sc bilayer periodicity is $\Lambda \approx 8.3 \text{ nm}$ and the average t_{Dy} is $\approx 8 \text{ ML}$. In addition, we observe the development of relatively sharp Dy-Sc interfaces, where these appear slightly wavy. To some extent, HRTEM images seem to be fully consistent with XRD data. However, taking a closer look at the HRTEM image, it is observed a relatively good continuity of the $\{1\bar{1}02\}$ planes across the Dy-Sc interface. At first sight, this seems to be inconsistent with XRD data, which shows a differentiated a lattice parameter for Dy and Sc layers. Equally, the out-of-plane coherent strain $\varepsilon_{\perp} = -2\varepsilon_0 t_{\text{Sc}} c_{13}/c_{33} (c_c t_{\text{Dy}} + t_{\text{Sc}})$, calculated from the minimization [61] of the elastic energy associated to the Dy/Sc bilayer, yields larger values than those experimentally determined, where $c_c \approx 0.8$ is a complex ratio involving symmetric elastic constants for Dy and Sc. Partial relief of the epitaxial strain can be achieved by the onset of a network of misfit dislocation, which in hexagonal crystals are likely to be purely edge dislocations on the slip plane and direction $\{1\bar{1}02\}\langle 1\bar{1}20\rangle$, with a burger's vector $b = a_{\text{Dy}}/\sqrt{2}$. Thus, making use of the XRD data, we estimate that the linear spacing s of misfit dislocations [62], consistent with the partial relaxation of the coherent strain, should be $s = 3.3 \text{ nm}$, so that a number of dislocations should be visible in the HRTEM image. However, this seems not to be the case after inspecting a number of HRTEM images, as seen in Fig. 3(b). Although we can not absolutely confirm the absence of misfit dislocations, our observation is solid evidence that points to the presence of an alternative strain relief mechanism.

Disentangling the way and degree in which the epitaxial strain is relaxed in layered heterostructures is an intricate theme [63] for low misfits typically below 2%, and even more complex for misfits $>2\%$ above which the crystal potential is severely perturbed. Hauenstein *et al.* [64] showed that, under identical chemical composition/modulation and misfit conditions, the epitaxial growth of multilayered heterostructures results in a considerable smaller degree of strain

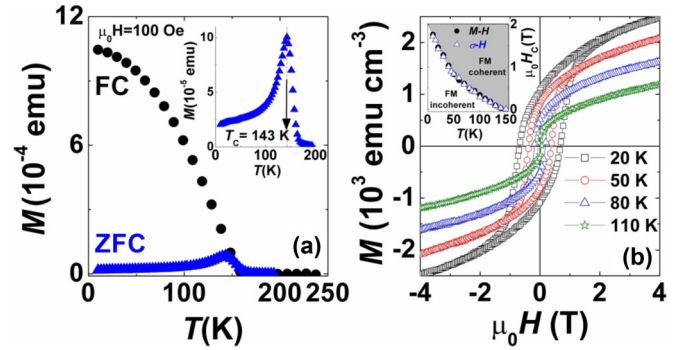


FIG. 4. (Color online) For the $\text{Dy}_{20}/\text{Sc}_{60}$ SL. (a) Zero-field-cooled (ZFC) and field-cooled (FC) magnetization curves. Inset graph is a magnification of the ZFC curve around T_c . (b) Hysteresis loops at representative temperatures. Inset graph shows a magnetic phase diagram for the low- H incoherent to high- H coherent ferromagnetic structure. The critical fields H_{cr} are obtained from magnetization (full circles) and magnetoelastic stress (empty triangles) curves. In both cases, the applied magnetic field \mathbf{H} is along the in-plane easy direction.

relief than in the case of alike bilayer/overlayer counterparts. Moreover, the critical thickness h_c above which the strained film grows incoherently by introducing misfit dislocations is found ≈ 3 times larger in bilayers than in single layers [65]. A more recent study on the pseudoepitaxial growth of high lattice-mismatched heterostructures has shown the pronounced tensile-compressive asymmetry [66], wherein the h_c is found to be a few monolayers under compression, for instance, Huang *et al.* [67] found $h_c \approx 3 \text{ ML}$, and 9 ML under tensile strain. Building on the above arguments, we can conclude that the formation of a misfit dislocation network in the case of Dy/Sc SLs may be prevented by the combination of two factors, the multilayer structure effect and the large tensile-compressive asymmetry, so that for the Dy layers $h_c > t_{\text{Dy}} \approx 8 \text{ ML}$, in good accord with our experimental findings. An alternative strain relief mechanism observed during the growth of high lattice-mismatched [69] heterostructures consists of the development of a corrugated phase [68], which would be consistent with the slight wavy appearance of the interfaces in the Dy/Sc SLs, as shown in Fig. 3(b).

B. Magnetization and vector magnetometry: Magnetic anisotropy constants

ZFC and FC M - T curves are very similar for all four $[\text{Dy}_{20} \text{ \AA} / \text{Sc}_m]_{50}$ SLs. In Fig. 4, zero-field cooled (ZFC) and field-cooled (FC) M - T curves for a representative SL are displayed, which show no trace of the cusplike feature characteristic of the onset of the c -plane spin-spiral antiferromagnetic (AFM) phase that forms in bulk Dy [70] below 179 K. Additionally, the FC M - T curve shows a typical decay as temperature increases found in ferromagnets and the ZFC one present a pronounced and asymmetric peak at the Curie temperature $T_c^{\text{SL}} = 143 \text{ K}$. The pronounced irreversibility shown by ZFC and FC M - T curves is incompatible with the onset of coherent FM stack in the Dy/Sc SL. Prior neutron scattering experiments conducted in similar Dy/Sc [71] and strained-alike Ho/Sc [33] SLs showed that magnetic moments

lie in the basal plane and the short-range coherence of the magnetic structure developed in the SL, so that in the Dy/Sc SLs the coherent along the growth direction of the FM structure is equal to the Dy layer thickness. These two evidences strongly suggest that coherent FM order is exclusively confined to Dy layers in the same block, whereas Dy layers belonging to adjacent blocks are very weakly coupled or present no coupling at all through the nonmagnetic Sc spacer layers [72].

Hysteresis loops show a close resemblance to those typically found in a collection of noninteracting ferromagnetic single-domain particles [73] [see Fig. 4(b)]. Thus, we find that the remanence magnetization is half the magnetization value reached when the M - H loop is completely closed and, as H is further increased beyond that point, M keeps on increasing steadily. These two features are clear fingerprints of the onset of an incoherent FM phase in Dy/Sc SLs, where adjacent Dy blocks are magnetically decoupled through the Sc ones. Figure 4(b) shows the H - T magnetic phase diagram, collected from ZFC M - H and σ - H curves, which displays the low-field incoherent and a high-field coherent FM phase.

In analogy to the spin-spiral magnetic phase developed in strained-alike Ho/Lu SLs [74], we would expect a shift towards a larger period in the spin-spiral AFM structure in the Dy/Sc SL, λ_{AF}^{SL} , so that $\lambda_{AF}^{SL} > \lambda_{AF}^{Dy}$, where λ_{AF}^{Dy} is the period of the helixlike structure in bulk Dy [70], which varies from ~ 8.2 MLs at T_N up to ~ 14 MLs right before T_C . The suppression of the helical magnetic phase can be attributed to two different factors or a combination of both: (1) The ultrathin nature [75] of the Dy layers would eventually prevent to stabilize the spin-spiral magnetic structure [76] in the Dy layers, given that $t_{Dy} \approx 8$ MLs $\leq \lambda_{AF}^{SL}$ and (2) as previously noted [33], the electronic band structure in the Dy/Sc SL may differ from that of the constituent metallic species as a result of the chemical modulation and epitaxial strain, so that the conduction electron susceptibility lacks of a maximum at an ordering wave vector $\mathbf{Q} \neq 0$ [77].

The low dimensionality of the Dy layers has two opposite effects upon the FM ordering temperature. On one hand, because of the long range of the indirect-exchange [78] coupling, the magnetic properties of RE-based nanostructures [75] are heavily affected by the finite-size effect. This way, we observe that for $t_{Dy} \sim 8$ MLs, the dependence of T_C on film thickness [79] predicts a variation in the ordering temperature, which amounts to $\Delta T_C \approx -36$ K in Dy/Sc SLs, in comparison to $T_C (= 89$ K) in bulk Dy [70]. On the other hand, it is well established that the epitaxial compression strain shifts the FM ordering transition towards higher temperature in RE-based [80,81] SLs. After considering both effects, we estimate that the epitaxial strain enhances T_C , so that, $\Delta T_C \approx 90$ K. Taking this value, we calculate that the Dy layers must be under an in-plane compression stress $\sigma_{\parallel} \approx 0.9$ GPa [82]. Now, considering that the out-of-plane epitaxial stress $\sigma_{\perp} = 0$, and assuming that, in first order of approximation, the in-plane strain can be considered isotropic and c_{ij} for the Dy layers are similar to those in Dy bulk [59], we estimate that $\varepsilon_{\parallel}^{\text{calc}} \approx 1.1\%$, which is almost half the experimental ε_{\parallel} , but still in relatively good accord with the light of the crude assumptions made.

Vector magnetometry is proven as an accurate technique to investigate the magnetic anisotropy in nanostructured matter

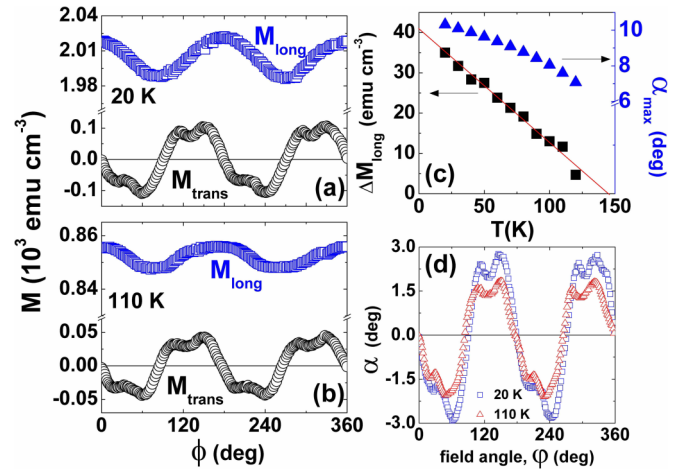


FIG. 5. (Color online) Longitudinal (black circles) M_{long} and transversal (blue squares) M_{trans} components of the total magnetization with respect to the applied magnetic field \mathbf{H} in the rotation plane, i.e., (0001), as a function of the crystal angle ϕ for the Dy₂₀/Sc₆₀ superlattice for $\mu_0 H = 2$ T at (a) $T = 20$ K and (b) $T = 110$ K. (c) Temperature variation of ΔM_{\parallel} and the calculated α , which would reproduce ΔM_{\parallel} . The line is a mere eye guide. (d) Dependence of the experimentally determined α on the field angle ϕ at representative temperatures. For further details, see text.

[83,84]. The collected $M_{\parallel}(\phi)$ and $M_{\perp}(\phi)$ show a number of features, which are consistently repeated across all four Dy/Sc SLs. For simplicity, magnetic torque measurements are illustrated by showing curves collected in a representative sample, that is, in [Dy₂₀/Sc₆₀]₅₀ SL. As shown in Fig. 5, M_{\parallel} and M_{\perp} present the following features: (1) M_{\parallel} shows a gentle oscillation, which presents a twofold symmetry, whereas M_{\perp} exhibits the superimposition of twofold and sixfold symmetries. (2) Crossings through zero with negative slope for M_{\perp} correspond to a maximum in M_{\parallel} , that is, easy direction for \mathbf{M} , and those with positive slope correspond to a minimum in M_{\parallel} , hard direction for \mathbf{M} . (3) We notice that $M_{\parallel} \gg M_{\perp}$, where the maximum ratio $M_{\perp}/M_{\parallel} \approx 0.05$ even at $T = 20$ K. This is a clear evidence of that $H \gg H_k$ at all times, where H_k is the anisotropy field, so that \mathbf{M} follows \mathbf{H} through the rotation and slightly deviates from \mathbf{H} while passing over the hard direction for \mathbf{M} .

Figure 5(c) displays the scaling with temperature for the oscillation amplitude shown by M_{\parallel} , that is, ΔM_{\parallel} , which is apparently caused by the lack of saturation of \mathbf{M} , according to the general wisdom [85], so that \mathbf{M} moves away from the \mathbf{H} direction while passing over the hard axis. However, we find that the calculated angle α_{max} , that reproduces ΔM_{\parallel} [see Fig. 5(c)], exceeds by far the angle α experimentally determined [see Fig. 5(d)]. This result alongside the fact that $H \gg H_k$ suggest a genuine origin for ΔM_{\parallel} . The \mathbf{M} anisotropy in RE metals is still a theme of controversy [86] and remains unsolved. Due to the strong spin-orbit [55] interaction, the indirect-exchange coupling in lanthanides should comprise isotropic and symmetric anisotropic terms [87,88], nonetheless, because this fact remains experimentally untested, the general wisdom [85] still stands unchallenged so far. Despite that dealing in depth with \mathbf{M} anisotropy is

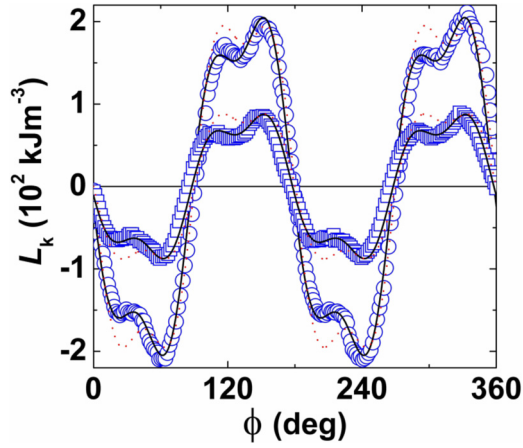


FIG. 6. (Color online) For the c -oriented $[\text{Dy}_{20}/\text{Sc}_{60}]_{50}$ SL. Experimental magnetic torque L_k as a function of the crystal angle ϕ for an in-plane applied magnetic field $\mu_0 H = 2$ T and at $T = 20$ K (circles) and $T = 110$ K (squares). The lines are a fit of L_k according to the following relationship: $L_k = 2K_2^{ef} \sin 2\phi + 6K_6^{ef,6} \sin 6(\phi + \phi_o)$, where $\phi_o = 5^\circ$ (continuous black line) and $\phi_o = 0$ (dotted red line). The best-fit parameters are $K_2^{ef} = -113 \text{ kJm}^{-3}$ and $K_6^{6,ef} = -8.3 \text{ kJm}^{-3}$ at $T = 20$ K and $K_2^{ef} = -42 \text{ kJm}^{-3}$ and $K_6^{6,ef} = -3.1 \text{ kJm}^{-3}$ at $T = 110$ K. Notice that $\phi = 0$ corresponds to the \mathbf{b} direction in the hcp lattice. For further details, see text.

beyond the scope of this paper, here we briefly point to the fact that vector magnetometry data collected in Dy/Sc SLs constitute a first evidence for \mathbf{M} anisotropy in RE systems, which is consistent with the proposed existence of anisotropic indirect-exchange [89] terms in lanthanides.

According to the symmetry exhibited by the experimental magnetic torque L_k in the Dy/Sc SLs, we propose a fitting relationship, which departs from prior studies [83] and reads as

$$L_k(\phi) = 2K_2^{ef} \sin 2\phi + 6K_6^{ef,6} \sin 6(\phi + \phi_o), \quad (9)$$

where we have included effective uniaxial K_2^{ef} and hexagonal $K_6^{ef,6}$ magnetic anisotropy constants, respectively, and ϕ_o is the shift angle between the uniaxial direction and the hexagonal lattice, to which K_2^{ef} and $K_6^{ef,6}$ are referred. The best fit of $L_k(T, H)$ is achieved by taking $\phi_o = 5^\circ$, as shown in Fig. 6. However, we notice that modeling L_k by taking $\phi_o = 0$ in Eq. (9) leads to a certain disagreement between experiment and model (see Fig. 6), although all major features in L_k are still reproduced. Now, notice that Eq. (9) yields a set of field dependent $K_2^{ef}(T, H)$ and $K_6^{ef,6}(T, H)$ constants and, therefore, in order to access to a generic field-independent magnetic anisotropy constant $K_n^l(T)$, we have followed a well-established procedure [90,91], which assumes that $K_n^l(T, H) \simeq K_n^l(T, \infty)(1 - C/\mu_0 H)$. Figure 7(a) shows the H -dependent anisotropy constants $K_2^{ef}(T, H)$ and $K_6^{ef,6}(T, H)$ and the extrapolated values to $H^{-1} = 0$.

The most outstanding feature unlocked by the magnetic torque experiments in Dy/Sc SLs is the arising of an in-plane uniaxial magnetic anisotropy, which strikingly outweighs the characteristic sixfold magnetic anisotropy and, therefore, determines the easy direction for \mathbf{M} , as shown in Fig. 6, in

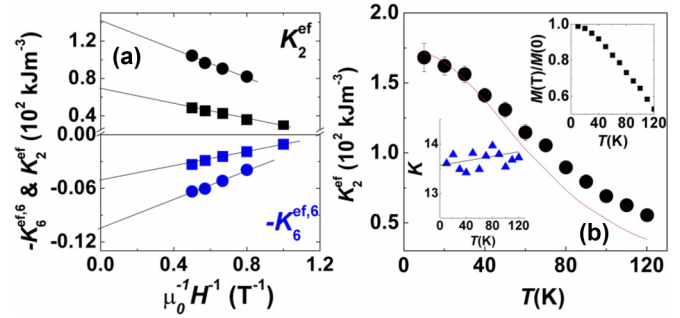


FIG. 7. (Color online) Data collected in the $\text{Dy}_{20}/\text{Sc}_{60}$ SL. (a) Extrapolation to $H = \infty$ of the uniaxial $K_2^{ef}(T, H)$ and hexagonal $K_6^{ef,6}(T, H)$ field-dependent anisotropy constants at $T = 40$ K (circles) and $T = 110$ K (squares) following the standard procedure [90,91]. (b) Temperature dependence of the uniaxial magnetic anisotropy constant K_2^{ef} . The continuous line is a fit according to the single-ion model [93], so that, $K_2^{ef}(T) = K_2^{ef}(0) \hat{I}_{5/2}[\mathcal{L}^{-1}(m)]$ where $K_2^{ef}(0) = 175 \text{ kJm}^{-3}$, $\hat{I}_{5/2}[\mathcal{L}^{-1}(m)]$ is the reduced hyperbolic Bessel function, \mathcal{L}^{-1} is the inverse Langevin function, and $m = M(T)/M(0)$ is the reduced magnetization (see top inset graph), where $M(0)$ is the extrapolated to $T = 0$ K for the T -dependent high-field magnetization $M(T)$. Bottom inset graph shows the ratio $K = K_2^{ef}/K_6^{ef,6}$, where the line is a linear fit, so that, $K(T) = K(0) - 0.0022T$, where $K(0) = 13.56$.

clear contrast to bulk Dy [92]. It is well established [55] that the magnetic anisotropy in RE metals is due to the interaction between the highly anisotropic orbital moment of the unfilled $4f$ shell and the crystal field created by the metallic lattice. The single-ion model developed by Callen *et al.* [93] provides a satisfactory account for the temperature scaling of the magnetic anisotropy in bulk RE [55,92] metals, as well as in RE-based [83] SLs. However, we observe that in the ultrathin Dy/Sc SLs, the single-ion [93] model achieves a moderate success, matching the experimental data in the low- T range, i.e., for $T \leq T_C^{\text{SL}}/3$, while slightly underestimating K_2^{ef} for higher temperatures, as shown in Fig. 7(b). This discrepancy may be due to the finite size of the Dy layers and further work to clarify this point is underway. Now, taking the $[\text{Dy}_{20}\text{Sc}_{60}]$ SL as example, the extrapolation of the magnetic anisotropy constants to $T = 0$ K yields $K_2^{ef}(0) = 175 \text{ kJm}^{-3}$ and $K_6^{6,ef}(0) = 13 \text{ kJm}^{-3}$, where the ratio $K = K_2^{ef}/K_6^{6,ef} \approx 13.5$ and varies very little as temperature rises [see Fig. 7(b)]. Notice that, for consistency, we have adopted the bulk's criteria, where $K_6^6 < 0$, so that \mathbf{a} is the easy direction for \mathbf{M} in bulk Dy. Importantly, we highlight that comparing to M in bulk Dy. Importantly, we highlight that comparing to $K_6^6 (= -0.76 \text{ MJm}^{-3})$ in bulk Dy [92], $K_6^{6,ef}$ is not only a small fraction when compared to K_6^6 but, in addition, $K_6^{6,ef} > 0$ and K_2^{ef} is nearly one-fourth of K_6^6 in absolute terms. In a wider context, $K_6^{6,ef}$ is similar to K_1 in Fe_3O_4 [3] and K_2^{ef} is comparable to K_1 in Gd [3].

We attribute the extraordinary decreasing and sign reversing of $K_6^{6,ef}$ to the arising of a competing sixfold MEL anisotropy term $K_{6, \text{MEL}}^6$, which stems from the symmetric lattice distortion generated by the epitaxial stress [83]. The physical origin of this change resides on the homogenization of the crystal field (CF) generated by the metallic lattice under an in-plane compression stress, which reflects on the fact that the CF is

effectively screened by the conduction electrons [94]. Strains in thin films and multilayers are essentially due to a *morphic* origin, that is, induced by the epitaxial misfit and/or thermal stress, and a *magnet* origin (magnetostriction), e.g., induced by the rearrangement of the magnetic moments. Because of the clamping exerted by substrate, buffer, and/or interleaved layers, the former mostly dominate. Thus, in terms of the *morphic* α strains $\varepsilon_{\alpha 1}$ and $\varepsilon_{\alpha 2}$ associated to the fully symmetric representation in hexagonal symmetry [54] and, assuming a linear model, the strain-dependent $K_6^{6,ef}$ can be written as [51,83],

$$K_6^{6,ef} = K_6^6 - (M_{\alpha 1}^{66}\varepsilon_{\alpha 1} + M_{\alpha 2}^{66}\varepsilon_{\alpha 2}), \quad (10)$$

where K_6^6 is the sixfold magnetocrystalline (unstrained) anisotropy constant and $K_{6,MEL}^6 = -(M_{\alpha 1}^{66}\varepsilon_{\alpha 1} + M_{\alpha 2}^{66}\varepsilon_{\alpha 2})$, so that the sixfold α -MEL constants are defined as $M_{ai}^{66} \equiv \frac{\partial K_6^6}{\partial \varepsilon_{ai}}|_{\varepsilon_{ai}=0}$. We should notice that if nonlinear effects are present, these will be included in the MEL constants.

At this point, it is interesting to obtain an estimation of $M_{\alpha 1,2}^{66}$ in bulk Dy. To that purpose, we have used the forced α striction, defined as $\varepsilon_{\alpha 1,2}^{for} = \varepsilon_{\alpha 1,2}^H - \varepsilon_{\alpha 1,2}^0$, where $\varepsilon_{\alpha 1,2}^H$ is the field-induced magnetostriction (MS) in the fully magnetized phase and $\varepsilon_{\alpha 1,2}^0$ is the zero-field MS, which can be related to $M_{\alpha 1,2}^{66}$, as follows [51]: $\varepsilon_{\alpha 1,2}^{for} = (M_{\alpha 1,2}^{66}c_{\alpha 2,1} - M_{\alpha 2,1}^{66}c_{\alpha 3})c_{\alpha}^{-1}\cos 6\phi$, where $c_{\alpha j}$ and c_{α} are symmetric elastic constants in hexagonal symmetry [54]. By manipulating the linear magnetostrictions [55,95], we have obtained $\varepsilon_{\alpha 1,2}^{for}$, and using the T dependent c_{ij} in bulk Dy [59], we have determined $M_{\alpha 1,2}^{66}$. We will use the extrapolated values to $T = 0$ K, which are $M_{\alpha 1}^{66} = -0.68$ GPa and $M_{\alpha 2}^{66} = 0.29$ GPa. Now, assuming that $\varepsilon_{xx} \approx \varepsilon_{yy} = \varepsilon_{\parallel}$ and $\varepsilon_{zz} = \varepsilon_{\perp}$, we calculate that in the Dy₂₀/Sc₆₀ SL, $\varepsilon_{\alpha 1} = -0.0206$ and $\varepsilon_{\alpha 2} = 0.0281$, and using the above $M_{\alpha 1,2}^{66}(T = 0$ K), we obtain that $K_{6,MEL}^{6,calc} \approx -22$ MJm⁻³, which largely exceeds the experimental value in absolute terms $K_{6,MEL}^6 = 0.773$ MJm⁻³. Not surprisingly, this means that the strained state of the Dy layers has altered (diminished) $M_{\alpha 1,2}^{66}$, which emphasizes the need for including nonlinear effects due to the onset of large morphic strains $>1\%$. Therefore, in order to obtain an estimate, we will exploit the fact that in bulk Dy, the ratio $M_{\alpha 1}^{66}/M_{\alpha 2}^{66} \approx -2.3$ for $T \leq T_C$ and we will assume that such a trend is also replicated in Dy/Sc SLs.

Building on the MEL origin of $K_6^{6,ef}$ [see Eq. (10)], we can relate $K_{6,MEL}^6$ to t_{Sc} as follows:

$$K_{6,MEL}^6 = -|d^*|\varepsilon_{\perp}M_{\alpha 2}^{66} = -|d^*|M_{\alpha 2}^{66}[\varepsilon_{\perp}^o + \varepsilon_{\perp}(t_{Sc})], \quad (11)$$

where $\varepsilon_{\perp}^o = \varepsilon_{\perp}(t_{Sc} = 0)$ and the constant $d^* = 2.6(1 - c_{33}/c_{13}) - \sqrt{3}/2 \approx -9.5$. As shown in Fig. 8, $K_{6,MEL}^6$ presents a linearlike variation with the experimental ε_{\perp} , in good accord to Eq. (11). Notice that ε_{\perp}^o would correspond to the out-of-plane strain for a 100-nm-thick Dy layer deposited on a 120-nm-thick Sc layer, the resulting heterostructure when the limit $t_{Sc} \rightarrow 0$ is taken in the Dy/Sc SLs. By minimizing the elastic energy [61] of the Dy/Sc SL, it is straightforward to demonstrate that if t_{Dy} is left unchanged and t_{Sc} is varied, then this situation leads to $\varepsilon_{\perp} \approx \varepsilon_{\perp}^o + \varepsilon_1 t_{Sc}$, where the best-fit is achieved by taking $\varepsilon_{\perp}^o(\%) = 0.55 \pm 0.2$, as shown in Fig. 8(a). We also estimate that $K_{6,MEL}^6(\varepsilon_{\perp}^o) \approx -0.731$ MJm⁻³,

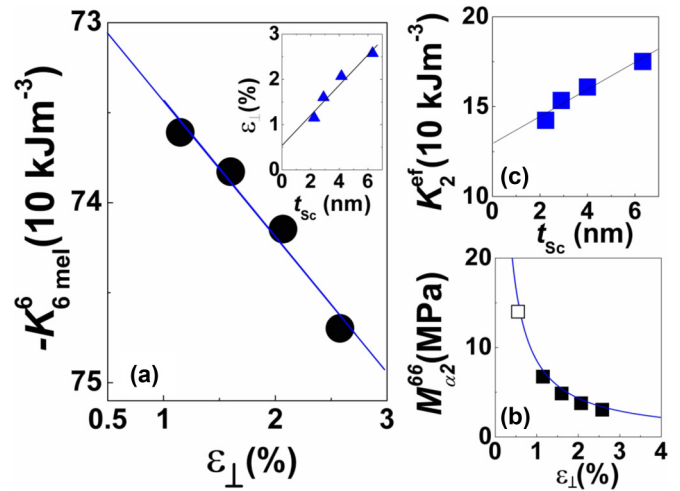


FIG. 8. (Color online) Dependence of the sixfold magnetoelastic anisotropy constant $K_{6,MEL}^6 = K_6^{6,ef} - K_6^6$, on the experimental out-of-plane strain ε_{\perp} , where $K_6^6 = -0.76$ MJm⁻³ is the bulk Dy sixfold magnetocrystalline anisotropy constant [92] and $K_6^{6,ef}$ is the measured one in the Dy/Sc SLs. The line is a mere eye guide. The inset graph shows a plot of ε_{\perp} with the Sc layer thickness t_{Sc} and a linear fit $\varepsilon_{\perp} = \varepsilon_{\perp}^o + \varepsilon_1 t_{Sc}$, where the best-fitting parameter are $\varepsilon_{\perp}^o = \varepsilon_{\perp}(t_{Sc}) = 0.55 \pm 0.2$ and $\varepsilon_1 = 0.33 \pm 0.05$ nm⁻¹. (b) Strain-dependent sixfold MEL constant $M_{\alpha 2}^{66}$, where full squares are experimental values and the empty one corresponds to the estimated $M_{\alpha 2}^{66}(\varepsilon_{\perp}^o) = 14$ MPa. The line is a nonlinear fit according to the equation $M_{\alpha 2}^{66} = M_{\alpha 2}^{66}(0)(1 + b\varepsilon_{\perp})^{-1}$, where the best-fit parameter is $b = 3200$. (c) Variation of the uniaxial magnetic anisotropy constant K_2^{ef} , with t_{Sc} . The line is a linear fit, so that $K_2^{ef} = K_2^{ef}(0) + k_1 t_{Sc}$, where the best-fit parameters are $K_2^{ef}(0) = (1.29 \pm 0.05) \times 10^2$ kJm⁻³ and $k_1 = (0.075 \pm 0.01) \times 10^5$ GJm⁻². For further details, see text.

obtained as a linear extrapolation. We can test the accuracy of the linear fit for $\varepsilon_{\perp}(t_{Sc})$, by producing an estimate for ε_{\perp}^o , which can be calculated as [96] $\varepsilon_{\perp}^o = -2\varepsilon_0 c_{13}/c_{33}(t_c/t_{Dy})$, where $\varepsilon_0 (= -0.079)$ and t_c is the critical thickness. Using the Basson and Ball model [97], an energy minimization leads to a simplified relationship for $t_c \approx a_{Dy}/2\varepsilon_0 \approx 2$ nm, so that we estimate that $\varepsilon_{\perp}^o \approx 0.3\%$, in relatively good accord with the linear fit. Now, plotting $M_{\alpha 2}^{66} (= -K_{6,MEL}^6/|d^*|\varepsilon_{\perp})$ against ε_{\perp} yields a nonflat but smooth dependence on ε_{\perp} , which underlies the importance of nonlinear effects, as shown in Fig. 8(a). For completeness, we have also included the calculated value for $M_{\alpha 2}^{66}(\varepsilon_{\perp}^o)$. Based on the experiment, we postulate that the strain modifies [98] $M_{\alpha 2}^{66}$ according to the following relationship:

$$M_{\alpha 2}^{66} = M_{\alpha 2}^{66}(0)(1 + b\varepsilon_{\perp})^{-1}, \quad (12)$$

where $M_{\alpha 2}^{66}(0) = 0.29$ GPa is the bulk value, and the best-fitting parameter is $b = 3200$. In this way, inserting $\varepsilon_{\perp} = -2\frac{c_{13}}{c_{33}}\varepsilon_{\parallel}$ in Eq. (12) and expanding the above nonlinear dependence around $\varepsilon_{\parallel} = 0$, we obtain a first-order MEL constant $N_{\alpha 2}^{66} \approx 490$ GPa, consistent with prior accounts [99,100]. As shown in Fig. 8(b), Eq. (12) provides a successful fit for $N_{\alpha 2}^{66}$, which yields a second-order approximated polynomial dependence on the strain for typically $\varepsilon < 0.2\%$, as prior studies found in RE-based [83] SLs and 3d-based [101] thin films. The

microscopic mechanism behind the strain-dependent MEL constants resides on their CF (single-ion) origin [102]. Thus, the strain modifies the local ionic bond strength, which in turn leads to a redistribution of the conduction electron band density, which results in a different screening of the distorted (strained) metallic lattice potential by the conduction electrons. It is remarkable that, contrary to $K_6^{6,ef}$, K_2^{ef} shows smooth increase as the Dy/Sc bilayer gets thicker, as seen in Fig. 8(c). A pseudophenomenological linear fit serves well the experimental data, which points to the most likely origin for the UMA is the developing of an in-plane anisotropic lattice parameter [28]. We stress that our analysis does not exclude beforehand that $M_{\alpha_2}^{66}$ and, by extent, to $K_6^{6,ef}$ and K_2^{ef} , might be contributed by volume and interface terms. However, the lack of a prior account for such sixfold interface terms in RE-based nanostructures and the structure of the examined Dy/Sc SLs, with a fix Dy layer thickness, makes it hard to efficiently separate them out.

C. Origin of the in-plane uniaxial anisotropy: Magnetoelastic constant $M_{\gamma,2}^2$

The epitaxial registry of dissimilar (0001)hcp layers deposited on (110)bcc surface reaches a minimum in elastic energy when the hcp overlayer undergoes an *anisotropic strain relaxation* [103]. Building on this evidence, we will explore whether the (0001)Sc seed layer, ~ 120 nm thick, deposited on (110)Nb is likely to develop an ASR process. If that is proven feasible, this would cause that the subsequent deposition of (0001)Dy/Sc multilayered structure encounters an orthorhombiclike distorted (0001) template surface, which is likely to be reconstructed by the ultrathin Dy/Sc bilayer and, subsequently, such anisotropic in-plane lattice parameter is likely to be enhanced as the deposited Dy/Sc multilayer grows thicker [28]. Therefore, the emergence of an in-plane γ strain $\varepsilon_{\gamma 1} = (\varepsilon_{xx} - \varepsilon_{yy})/2$ in the Dy/Sc SLs would generate a γ -MEL contribution to the MAE, where the associated UMA is given by

$$K_2^{ef} = -M_{\gamma,2}^2 \varepsilon_{\gamma,1}. \quad (13)$$

First, we will commence by determining the MEL constant that breaks the in-plane hexagonal symmetry $M_{\gamma,2}^2$, which may differ in nanostructured [98] Dy. To that end, longitudinal $\sigma(b,a)$ and transversal $\sigma(a,a)$ MEL stress loops σ - H were determined from T_C^l down to $T = 10$ K. σ - H loops present a butterflylike shape, typically featured by FM-like materials, in the low-field range and an unsaturated behavior in the high-field limit, consistent with M - H loops, as shown in Figs. 9(a) and 9(b). We observe a good correlation between M - H and σ - H loops, where both are closed at the same applied fields and the critical fields marking the transition between an incoherent FM arrangement into a coherent FM state, obtained from ZFC M - H and σ - H curves, are consistent with one another.

As shown in Sec. II, $M_{\gamma,2}^2$ is determined from Eq. (8) by taking the measured $\sigma(b,a)$ and $\sigma(a,a)$ values for H well above H_k , for which the M - H loop is close. Notice that, because of the small in-plane sixfold magnetic anisotropy, it makes no difference whether $\mathbf{H} \parallel \mathbf{a}$ or $\mathbf{H} \parallel \mathbf{b}$, although we have typically taken the maximum applied field $\mu_0 H = 12$ T. Figure 9 shows the temperature scaling for $M_{\gamma,2}^2$, from which we estimate that

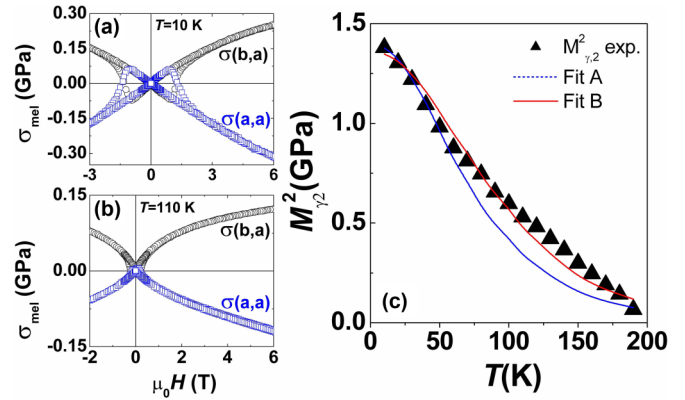


FIG. 9. (Color online) Magnetoelastic (MEL) stress loops $\sigma_{\text{MEL}}-H$ for a Dy₂₀/Sc₆₀ SL at (a) $T = 10$ K and (b) $T = 110$ K. $\sigma(b,a)$ and $\sigma(a,a)$ correspond to the longitudinal and transversal σ_{MEL} with respect to the applied magnetic field direction $\mathbf{H} \parallel \mathbf{a}$. (c) Temperature dependence of the symmetry-breaking magnetoelastic (MEL) constant $M_{\gamma,2}^2$. Lines are the best fit of $M_{\gamma,2}^2$ for two different approaches: (1) dashed line, fit A, corresponds to the single-ion model [54], so that $M_{\gamma,2}^2 = M_{\gamma,2}^2(0) \widehat{I}_{5/2}[\mathcal{L}^{-1}(m)]$ and (2) continuous line, fit B, corresponds to $M_{\gamma,2}^2 = M_{\gamma,2}^2(0)m^2$, where $M_{\gamma,2}^2(0) = 1.42$ GPa and $\widehat{I}_{5/2}[\mathcal{L}^{-1}(m)]$ is the reduced hyperbolic Bessel function, \mathcal{L}^{-1} is the inverse Langevin function, and $m = M(T)/M(0)$ is the reduced magnetization (see text for further details).

the extrapolated value at $T = 0$ K is $M_{\gamma,2}^2(0) = 1.42$ GPa, which means a nearly fourfold increase with respect to that in bulk Dy, $M_{\gamma,2}^{2,b} = 0.375$ GPa [29]. It is well established that the MEL coupling is modified by the thickness and/or strained state of thin films [98], as previously shown in RE-based [50] SLs.

The temperature dependence of $M_{\gamma,2}^2$ reflects on its microscopic origin [50]. It is important to notice that, because of the clamping [36] exerted by the sapphire substrate and the extraordinary adhesion [104] shown by the deposited metallic overlayers, the elastic properties of the bimorph are massively influenced by the substrate. Thus, we find that the thermal dependence for ε_{\parallel} is given by $\varepsilon_{\parallel}(T) \approx \varepsilon_{\parallel}(T = 300 \text{ K})(1 - \alpha_{\text{Al}_2\text{O}_3} \Delta T)$ where $\alpha_{\text{Al}_2\text{O}_3}$ is the thermal expansion coefficient for sapphire [105] single crystal, which implies that ε_{\parallel} varies very slowly with temperature. Therefore, we can consider in good approximation that the temperature dependence of all volumelike contributions [50] to $M_{\gamma,2}^2$ are well modeled by the Callen's theory of magnetostriction [54] (CTM). As shown in Fig. 9, CTM [54] provides a good fitting for $M_{\gamma,2}^2(T)$ exclusively in the low- T range, which suggests that interface contributions may play a significant part in the magnetoelastic properties of ultrathin Dy/Sc SLs. Unfortunately, a fixed Dy layer thickness in Dy/Sc SLs prevents to accurately explore interface contributions [106]. However, $M_{\gamma,2}^2$ is better accounted for by employing a fitting function, which goes as $M_{\gamma,2}^2(0)m^2$ [107], where m is reduced magnetization (see Fig. 9).

Nb thin films [108–110] grow on the sapphire substrate forming a highly ordered crystal structure with large coherence lengths and almost strain free. Indeed, the residual epitaxial strain is usually less than 0.05%, in good accord to our XRD

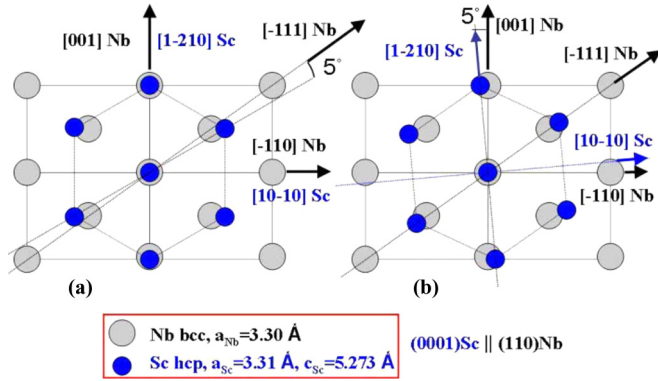


FIG. 10. (Color online) Schematic drawing of the epitaxial registry of (0001)Sc on (110)Nb according to (a) Kwo *et al.* [18] and (b) following the so-called Nishiyama-Wasserman [112] orientation.

scans in Dy/Sc SLs. We will therefore assume that for a Nb layer 50 nm thick, the in-plane lattice parameter is relaxed to the bulk value. The alignment between high-symmetry directions at the pseudoeptaxial growth of dissimilar (0001)hcp and (110)Nb layers was first elucidated by Kwo *et al.* [18,111], who found that the most densely packed rows of the Sc lattice are parallel to the densely packed [001] rows of the Nb one, and, consequently, the [10 $\bar{1}0$] direction of Sc is parallel to the [1 $\bar{1}0$] of Nb, as shown in Fig. 10(a). However, it is well established that the orientation of (0001)hcp deposited on (110)bcc should follow the so-called Nishiyama-Wasserman [112] orientation, which is slightly different, as seen Fig. 10(a). This would explain why a 5° shift is needed in order to achieve a perfect match between the model and the experimental L_k curves (see Sec. III B).

In order to obtain an estimate for the in-plane orthorhombic distortion, we will start assuming the epitaxial alignment shown in Fig. 10(a), for obvious reasons. Thus, along the Nb[001] direction, the interatomic spacing is $d_{\text{Nb}}^{[001]} = a_{\text{Nb}} = 3.30$ Å and along the [1 $\bar{2}10$]Sc, the interatomic spacing is $d_{\text{Sc}}^{[1\bar{2}10]} = a_{\text{Sc}} = 3.31$ Å. Bearing in mind that the misfit ε is calculated in a Sc-Sc bond with respect to the Sc-Sc separations in a bulk (0001)Sc layer, we obtain that $\varepsilon^{[1\bar{2}10]} = (d_{\text{Nb}}^{[001]} - d_{\text{Sc}}^{[1\bar{2}10]})/d_{\text{Sc}}^{[1\bar{2}10]} = -0.3\%$. Likewise, along the Nb[1 $\bar{1}0$] direction, the interatomic spacing is $d_{\text{Nb}}^{[1\bar{1}0]} = \sqrt{2}a_{\text{Nb}} = 4.667$ Å and along the [10 $\bar{1}0$]Sc, this is $d_{\text{Sc}}^{[10\bar{1}0]} = \sqrt{3}a_{\text{Sc}} = 5.733$ Å, so that $\varepsilon^{[10\bar{1}0]} = (d_{\text{Nb}}^{[1\bar{1}0]} - d_{\text{Sc}}^{[10\bar{1}0]})/d_{\text{Sc}}^{[10\bar{1}0]} = -18.6\%$, which is substantially larger than $\varepsilon^{[1\bar{2}10]}$. As observed in Fig. 11, the large $\varepsilon^{[10\bar{1}0]}$ does not prevent the coherent registry of (0001)Sc on (110)Nb, which presents a critical thickness $h_c = 7.2$ nm, typical of pseudomorphic growth under low lattice misfit.

Domain match epitaxy [113,114] (DME) model is a generalization of the conventional lattice match epitaxy, which has proven successful in accounting for the epitaxial growth of a broad range of high lattice-mismatched layered heterostructures [115,116]. Applying the DME [113,114] model to the growth of Sc on (110)Nb, we calculate that $\varepsilon^{[10\bar{1}0]}$ can be notably relaxed by forming two domain matching sets Nb:Sc, so that the first consists of 5 planes of Nb matching 4 planes of Sc, in short 5:4, and the second domain 6:5.

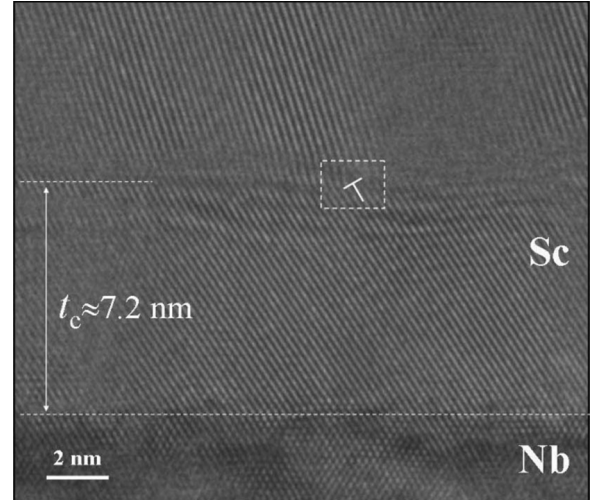


FIG. 11. HRTEM image of the Sc seed layer (top light gray color layer) on Nb (bottom dark gray color layer) at the [1 $\bar{2}10$] and [001] zone-axis orientations, respectively. The bottom white dashed line marks the (110)Nb/(0001)Sc interface. The localization of a misfit edge dislocation ($b=a_{\text{Sc}}/\sqrt{2}$) has been highlighted and a critical thickness of $h_c \approx 7.2$ nm is observed.

The residual strain for the domain matching 5:4 is $\varepsilon_{\text{DME}}^{5:4} = (5d_{\text{Nb}}^{[1\bar{1}0]} - 4d_{\text{Sc}}^{[10\bar{1}0]})/4d_{\text{Sc}}^{[10\bar{1}0]} = 1.7\%$, and for the domain 6:5 is $\varepsilon_{\text{DME}}^{6:5} = -2.3\%$. Alternating Nb:Sc domains with 5:4 and 6:5 matchings, with a frequency $\frac{2}{3}$, respectively, leads to an even lower residual (average) strain $\varepsilon_{\text{DME}}^{\text{avg}} = (2\varepsilon_{\text{DME}}^{5:4} + 3\varepsilon_{\text{DME}}^{6:5})/5 = -0.672\%$. Therefore, we show that applying the DME model to the epitaxial growth of (0001)Sc on (110)Nb leads to an ASR, where the strain for the first ≈ 26 MLs of Sc, i.e., below h_c , along the [1 $\bar{2}10$] and [10 $\bar{1}0$] directions becomes anisotropic, so that $\varepsilon_{\text{Sc}}^{[1\bar{2}10]} = -0.3\%$ and $\varepsilon_{\text{Sc}}^{[10\bar{1}0]} = -0.075\%$, respectively.

At this point, it is interesting to estimate the degree of relaxation of the anisotropic strain at the top of the Sc seed layer. We will calculate the strain relaxation with film thickness $\varepsilon_{\text{Sc}}(t_{\text{Sc}})$ by using the following power dependence [96]:

$$\varepsilon_{\text{Sc}} = \eta(t_c/t_{\text{Sc}})^{2/3}, \quad (14)$$

where $\eta(=\varepsilon_{\text{Sc}}^{[1\bar{2}10]}$ or $\varepsilon_{\text{Sc}}^{[10\bar{1}0]}$), $t_{\text{Sc}} = 120$ nm, and t_c is the critical thickness ≈ 7.2 nm. Thus, using Eq. (14), we estimate that the average strain for the 120-nm-thick Sc layer along the [1 $\bar{2}10$] and [10 $\bar{1}0$] directions is $\varepsilon_{\text{Sc,av}}^{[1\bar{2}10]} = -0.04596\%$ and $\varepsilon_{\text{Sc,av}}^{[10\bar{1}0]} = -0.01142\%$. We have opted for the $(1/t)^{2/3}$ power dependence for the strain relaxation *versus* thickness obtained by Ha *et al.* [96] because it produces a very similar thickness dependence than that derived from the Basson and Ball [97] model, with the additional advantage that is simpler and easier to model. Therefore, we have proven that the deposited Dy layers on the Sc seed layer will experience an anisotropic lattice misfit. The Dy layers will find ways to accommodate the large misfit, however, given that $\varepsilon_0 \gg \varepsilon_{\text{Sc,av}}^{[1\bar{2}10]}, \varepsilon_{\text{Sc,av}}^{[10\bar{1}0]}$, in first-order approximation we can assume that the strain relaxation in the Dy/Sc multilayer will be mostly isotropic as the number of Dy/Sc bilayers increase since both have hcp lattice structures.

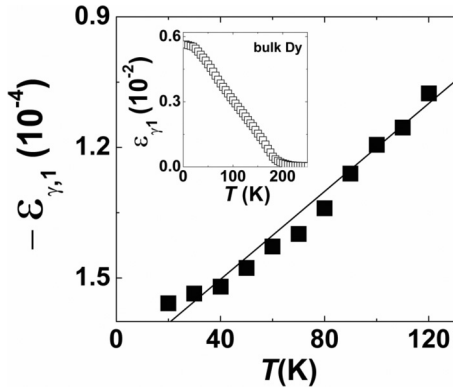


FIG. 12. Variation with temperature of the in-plane orthorhombiclike strain $\varepsilon_{\gamma,1}$ for the $[\text{Dy}_{20}\text{\AA}/\text{Sc}_{60}\text{\AA}]_{50}$ SL. The straight line corresponds to a linear fit, where the slope is $\approx 5 \times 10^{-7} \text{ K}^{-1}$. Inset graph shows $\varepsilon_{\gamma,1}$ for bulk Dy, obtained from existing linear magnetostriction data [55,95].

Building on this argument, it is straightforward to calculate that the Dy layers will develop an average orthorhombiclike distortion $\varepsilon_{\gamma,1}^{\text{cal}} = (\varepsilon_{\text{Dy}}^{[1\bar{2}10]} - \varepsilon_{\text{Dy}}^{[10\bar{1}0]})/2 \approx -1.7 \times 10^{-4}$.

Experimentally, $\varepsilon_{\gamma,1}$ can be determined by taking $K_2^{\text{ef}}(T)$ and $M_{\gamma,2}^2(T)$ [106] [see Eq. (13)], which works out that the values extrapolated at $T = 0 \text{ K}$ yield 1.1, 1.42, 1.61, and 1.23 ($= -\varepsilon_{\gamma,1}/10^{-4}$) for increasing t_{Sc} , that is, $|\varepsilon_{\gamma,1}|$ poses a smooth increase as t_{Sc} does [28]. At the moment, it is not fully understood why the thicker Dy/Sc SL deviates from that trend. On the other hand, we observe that $\varepsilon_{\gamma,1}$ shows a gentle T -dependent scaling, as seen in Fig. 12, very similar to that for all four Dy/Sc SLs. Most importantly, we notice a dramatic downsizing in $\varepsilon_{\gamma,1}$, by almost a factor 10^2 when compared to its counterpart [29] in bulk Dy, and a sign reversing (see Fig. 12), which strongly suggests its origin resides on the epitaxy growth, rather than in the spin alignment, as occurs in bulk Dy [55,117]. We would like to stress that the application of the DME [113,114] model to determine the ASR at the Nb/Sc interface and a power law [96] for estimating the strain relief with the Sc layer thickness achieves an excellent agreement between the experimental $\varepsilon_{\gamma,1}$ and the calculated $\varepsilon_{\gamma,1}^{\text{cal}}$, so that the correct magnitude and sign are predicted. Finally, we notice that from the linear fit of the experimental $\varepsilon_{\gamma,1}$ (see Fig. 12), we obtain a slope of $\approx 5 \times 10^{-7} \text{ K}^{-1}$, in good accord with α_s [105] in the low-temperature range, which is clear evidence of the clamping effect exerted by the substrate.

IV. CONCLUSIONS

As a summary, we have combined high-resolution structural characterizations, mainly XRD and TEM, alongside magnetization, magnetostriction, and magnetic anisotropy data to

correlate large alterations in the magnetic response of highly lattice-mismatched Dy/Sc superlattices to epitaxy-driven lattice distortions. A common criteria to predict the impact that epitaxy-related MEL effects may have upon the MAE is based on the ratio of $|M_1 \varepsilon_1|$ to other strain-free contributions to MAE, where the critical strain above which MEL energy exceeds magnetocrystalline (MC) anisotropy is $\varepsilon_{c,1}^K = |K_b/M_1|$ [3], where M_1 is the relevant MEL constant that couples to the epitaxially induced ε_1 and K_b is the dominant MC or strain-free anisotropy constant. However, a generic situation includes fully symmetric and symmetry-breaking epitaxially induced lattice distortions, which rescale K_b and add up low-symmetry MEL terms to MAE, respectively, which can result in an unexpected rebalancing of the MAE.

The above-mentioned situation is exemplarily illustrated in Dy/Sc SLs, where we have found that the characteristic in-plane hexagonal magnetic anisotropy has reversed sign and yields values around about $\approx 13\text{--}24 \text{ kJm}^{-3}$ and the emergence of a dominant in-plane uniaxial magnetic anisotropy, which attains values ranging $\approx 175\text{--}143 \text{ kJm}^{-3}$. In addition, we show that the dramatic downsizing of the sixfold anisotropy is originated in the compression stress introduced into the Dy layers by the Sc ones, which induces a sixfold MEL term that competes to the magnetocrystalline (strain-free) contribution. Likewise, we demonstrate that the anisotropic strain relaxation of the in-plane lattice parameter at the Nb/Sc interface is transferred to the Dy/Sc multilayer causing an orthorhombiclike distortion of the hexagonal lattice $\varepsilon_{\gamma,1} \approx 10^{-4}$, which in turn generates the dominant MEL uniaxial magnetic anisotropy, as a result of the coupling to a giant MEL constant $M_{\gamma,2}^2 \approx 1 \text{ GPa}$. Not surprisingly, the temperature dependence of K_2^{ef} and $M_{\gamma,2}^2$ is only partially described by the Callen and Callen theory, which strongly suggests that interface terms may have a significant contribution. This aspect still remains as an open question and further work is in progress. Finally, this study sets out that epitaxially driven inverse MEL effects can potentially transform the magnetic anisotropy in multilayered nanostructures and, therefore, completely change their magnetic response. In particular, the arising of symmetry-breaking lattice distortions in nonmagnetic bottom layers in complex superstructures may have profound implications upon the magnetic properties of the on-top deposited magnetic multilayer.

ACKNOWLEDGMENTS

We would like to thank M. A. Ciria and J. I. Arnaudas for helpful discussions. This study was funded by the Spanish Ministry of Science and Innovation, the Engineering and Physical Science Research Council (EPSRC) in U. K., and the European Commission through the PEOPLE-programm (Contract No. MEIF-CT-2006-025693).

- [1] *Nanomagnetism*, edited by D. L. Mills and J. A. C. Bland (Elsevier, Amsterdam, 2006).
 [2] C. A. F. Vaz, J. A. C. Bland, and G. Lauhoff, *Rep. Prog. Phys.* **71**, 056501 (2008).

- [3] R. C. O'Handley, *Modern Magnetic Materials* (Wiley, New York, 2000).
 [4] S. Chikazumi, *Physics of Magnetism* (Wiley, New York, 1978).

- [5] C. Uiberacker, J. Zabloudil, P. Weinberger, L. Szunyogh, and C. Sommers, *Phys. Rev. Lett.* **82**, 1289 (1999).
- [6] U. Welp, V. K. Vlasko-Vlasov, X. Liu, J. K. Furdyna, and T. Wojtowicz, *Phys. Rev. Lett.* **90**, 167206 (2003).
- [7] D. Sander, W. Pan, S. Ouazi, J. Kirschner, W. Meyer, M. Krause, S. Müller, L. Hammer, and K. Heinz, *Phys. Rev. Lett.* **93**, 247203 (2004).
- [8] A. Winkelmann, M. Przybylski, F. Luo, Y. Shi, and J. Barthel, *Phys. Rev. Lett.* **96**, 257205 (2006).
- [9] D. Houssameddine *et al.*, *Nat. Mater.* **6**, 447 (2007).
- [10] C. Chappert and P. Bruno, *J. Appl. Phys.* **64**, 5736 (1988).
- [11] Y. B. Xu, D. J. Freeland, M. Tselepi, and J. A. C. Bland, *Phys. Rev. B* **62**, 1167 (2000).
- [12] O. Thomas, Q. Shen, P. Schieffer, N. Tournier, and B. Lépine, *Phys. Rev. Lett.* **90**, 017205 (2003).
- [13] H. Fritzsche, J. Kohlhepp, and U. Gradmann, *Phys. Rev. B* **51**, 15933 (1995).
- [14] R. Sellmann, H. Fritzsche, H. Maletta, V. Leiner, and R. Siebrecht, *Phys. Rev. B* **63**, 224415 (2001).
- [15] J. Prokop, D. A. Valdaitsev, A. Kukunin, M. Pratzner, G. Schönhense, and H. J. Elmers, *Phys. Rev. B* **70**, 184423 (2004).
- [16] J. Wenisch, C. Gould, L. Ebel, J. Storz, K. Pappert, M. J. Schmidt, C. Kumpf, G. Schmidt, K. Brunner, and L. W. Molenkamp, *Phys. Rev. Lett.* **99**, 077201 (2007).
- [17] M. Ciria, F. J. Castaño, J. L. Diez-Ferrer, J. I. Arnaudas, B. G. Ng, R. C. O'Handley, and C. A. Ross, *Phys. Rev. B* **80**, 094417 (2009).
- [18] J. Kwo, M. Hong, and S. Nakahara, *Appl. Phys. Lett.* **49**, 319 (1986).
- [19] J. Kwo, E. M. Gyorgy, D. B. McWhan, M. Hong, F. J. DiSalvo, C. Vettier, and J. E. Bower, *Phys. Rev. Lett.* **55**, 1402 (1985).
- [20] C. F. Majkrzak *et al.*, *Adv. Phys.* **40**, 99 (1991).
- [21] J. J. Rhyne and R. W. Erwin, in *Handbook of Magnetic Materials*, edited by K. H. Buschow, Vol. 8 (North Holland, Amsterdam, 1995).
- [22] K. Y. Yang, H. Homma, and I. K. Schuller, *J. Appl. Phys.* **63**, 4066 (1988).
- [23] A. Stenborg, J. N. Andersen, O. Björneholm, A. Nilsson, and N. Martensson, *Phys. Rev. Lett.* **63**, 187 (1989).
- [24] K. M. Döbrich, M. Wietstruk, J. E. Prieto, F. Heigl, O. Krupin, K. Starke, and G. Kaindl, *Phys. Rev. Lett.* **100**, 227203 (2008).
- [25] K. M. Döbrich, A. Bostwick, J. L. McChesney, K. Rossnagel, E. Rotenberg, and G. Kaindl, *Phys. Rev. Lett.* **104**, 246401 (2010).
- [26] E. D. Tober, R. X. Ynzunza, C. Westphal, and C. S. Fadley, *Phys. Rev. B* **53**, 5444 (1996).
- [27] G. Piaszenski, R. Göbel, C. Jensen, and U. Köhler, *Surf. Sci.* **454–456**, 712 (2000).
- [28] G. Saraf, Y. Lu, and T. Siegrist, *Appl. Phys. Lett.* **93**, 041903 (2008).
- [29] L. Benito, J. I. Arnaudas, M. Ciria, C. de la Fuente and A. del Moral, *J. Phys.: Condens. Matter* **16**, 7151 (2004).
- [30] S. Legvold, J. Alstad, and J. Rhyne, *Phys. Rev. Lett.* **10**, 509 (1963).
- [31] R. C. C. Ward, M. R. Wells, C. Bryn-Jacobsen, R. A. Cowley, D. F. McMorrow, and J. A. Simpson, *Thin Solid Films* **275**, 137 (1996).
- [32] D. F. McMorrow, P. P. Swaddling, R. A. Cowley, R. C. C. Ward, and M. R. Wells, *J. Phys.: Condens. Matter* **8**, 6553 (1996).
- [33] C. Bryn-Jacobsen, R. A. Cowley, D. F. McMorrow, J. P. Goff, R. C. C. Ward, and M. R. Wells, *Phys. Rev. B* **55**, 317 (1997).
- [34] V. Oderno, C. Dufour, K. Dumesnil, A. Mougin, Ph. Mangin, and G. Marchal, *Philos. Mag. Lett.* **78**, 419 (1998).
- [35] L. Benito, J. I. Arnaudas, and A. del Moral, *Rev. Sci. Instrum.* **77**, 025101 (2006).
- [36] E. Klokholm, *IEEE Trans. Magn.* **12**, 819 (1976).
- [37] K. Twarowski and H. K. Lachowicz, *Phys. Status Solidi A* **53**, 599 (1979).
- [38] H. Awano, Y. Suzuki, T. Yamazaki, T. Katayama, and A. Itoh, *IEEE Trans. Magn.* **26**, 2742 (1990).
- [39] Macor technical datasheet, <http://www.cornis.com/macor>.
- [40] R. Watts, M. R. J. Gibbs, W. J. Karl, and H. Szymczak, *Appl. Phys. Lett.* **70**, 2607 (1997).
- [41] A. Ballato, *IEEE Trans. Ultrason. Ferroelectr. Freq. Control* **43**, 56 (1996).
- [42] B. T. Bernstein, *J. Appl. Phys.* **34**, 169 (1963).
- [43] W. E. Tefft, *J. Res. Natl. Bur. Stand., Sect. A* **70**, 277 (1966).
- [44] A. G. Every, G. L. Koos, and J. P. Wolfe, *Phys. Rev. B* **29**, 2190 (1984).
- [45] G. G. Stoney, *Proc. R. Soc. A* **82**, 172 (1909).
- [46] Capacitive Bridge-Model AH 2500A, <http://www.andeen-hagerling.com/ah2500a.htm>.
- [47] K. Dahmen, H. Ibach, and D. Sander, *J. Magn. Magn. Mater.* **231**, 74 (2001).
- [48] M. Ciria, J. I. Arnaudas, A. del Moral, M. R. Wells, and R. C. C. Ward, *Appl. Phys. Lett.* **72**, 2044 (1998).
- [49] J. J. Rhyne, S. Legvold, and E. T. Rodine, *Phys. Rev.* **154**, 266 (1967).
- [50] M. Ciria, J. I. Arnaudas, A. del Moral, G. J. Tomka, C. de la Fuente, P. A. J. de Groot, M. R. Wells, and R. C. C. Ward, *Phys. Rev. Lett.* **75**, 1634 (1995).
- [51] L. Benito, Ph.D. thesis, University of Zaragoza, 2004.
- [52] P. M. Marcus, *Phys. Rev. B* **53**, 2481 (1996); **54**, 3662 (1996).
- [53] A. del Moral, in *Handbook of Magnetism and Magnetic Materials*, edited by H. Kromüller and S. S. P. Parkin (Wiley, New York, 2007), Vol. 1, pp. 454–483.
- [54] E. R. Callen and H. B. Callen, *Phys. Rev.* **129**, 578 (1963); **139**, A455 (1965).
- [55] *Magnetic properties of Rare Earth Metals*, edited by R. J. Elliott (Plenum, London, 1972).
- [56] D. A. Jehan, D. F. McMorrow, R. A. Cowley, R. C. C. Ward, M. R. Wells, N. Hagmann, and K. N. Clausen, *Phys. Rev. B* **48**, 5594 (1993).
- [57] M. R. Khan, C. S. L. Chun, G. P. Felcher, M. Grimsditch, A. Kueny, C. M. Falco, and I. K. Schuller, *Phys. Rev. B* **27**, 7186 (1983).
- [58] D. Sander, *J. Phys.: Condens. Matter* **16**, R603 (2004).
- [59] S. B. Palmer, *J. Phys. Chem. Solids* **31**, 143 (1970).
- [60] M. L. Huberman and M. Grimsditch, *Phys. Rev. Lett.* **62**, 1403 (1989).
- [61] J. I. Arnaudas *et al.*, in *Frontiers in Magnetism of Reduced Dimensions Systems*, edited by V. G. Baryakhtar, P. E. Wigen and N. A. Lesnik (Kluwer Academic, Dordrecht, 1998), p. 525.
- [62] J. Y. Tsao, *Materials Fundamentals of Molecular Beam Epitaxy* (Academic, New York, 1993), p. 164.
- [63] D. J. Duncan, *J. Mater. Sci.: Mater. Electron.* **8**, 337 (1997).
- [64] R. J. Hauenstein, B. M. Clemens, R. H. Miles, O. J. Marsh, E. T. Croke, and T. C. McGill, *J. Vac. Sci. Technol. B* **7**, 767 (1989).

- [65] X. W. Liu, A. A. Hopgood, B. F. Usher, H. Wang, and N. St. J. Braithwaite, *Semicond. Sci. Technol.* **14**, 1154 (1999).
- [66] Y. Lu, M. Przybylski, O. Trushin, W. H. Wang, J. Barthel, E. Granato, S. C. Ying, and T. Ala-Nissila, *Phys. Rev. Lett.* **94**, 146105 (2005).
- [67] S. H. Huang, G. Balakrishnan, A. Khoshakhlagh, A. Jallipalli, L. R. Dawson, and D. L. Huffaker, *Appl. Phys. Lett.* **88**, 131911 (2006).
- [68] *Nano-optoelectronics*, edited by M. Grundmann (Springer, Berlin, 2003).
- [69] A. M. Bittner, J. Winterlin, and G. Ertl, *Surf. Sci.* **376**, 267 (1997).
- [70] M. K. Wilkinson, W. C. Koehler, E. O. Wollan, and J. W. Cable, *J. Appl. Phys.* **32**, S48 (1961).
- [71] F. Tsui, C. Uher, and C. P. Flynn, *Phys. Rev. Lett.* **72**, 3084 (1994).
- [72] F. Tsui, C. P. Flynn, R. S. Beach, J. A. Borchers, R. W. Erwin, and J. J. Rhyne, *J. Appl. Phys.* **73**, 6904 (1993).
- [73] E. C. Stoner and E. P. Wohlfarth, *Philos. Trans. R. Soc. London A* **240**, 599 (1948).
- [74] P. P. Swaddling, D. F. McMorrow, J. A. Simpson, M. R. Wells, R. C. C. Ward, and K. N. Clausen, *J. Phys.: Condens. Matter* **5**, L481 (1993); P. P. Swaddling, R. A. Cowley, R. C. C. Ward, M. R. Wells, and D. F. McMorrow, *Phys. Rev. B* **53**, 6488 (1996).
- [75] F. Cinti, A. Cuccoli, and A. Rettori, *Phys. Rev. B* **78**, 020402(R) (2008).
- [76] E. Weschke *et al.*, *Phys. Rev. Lett.* **93**, 157204 (2004).
- [77] W. E. Evenson and S. H. Liu, *Phys. Rev. Lett.* **21**, 432 (1968).
- [78] T. Kasuya, in *Magnetism*, edited by G. T. Rado and H. Suhl (Academic, New York, 1966), Vol. IIB.
- [79] R. Zhang and R. F. Willis, *Phys. Rev. Lett.* **86**, 2665 (2001).
- [80] R. S. Beach, J. A. Borchers, A. Matheny, R. W. Erwin, M. B. Salamon, B. Everitt, K. Pettit, J. J. Rhyne, and C. P. Flynn, *Phys. Rev. Lett.* **70**, 3502 (1993).
- [81] F. Tsui and C. P. Flynn, *Phys. Rev. Lett.* **71**, 1462 (1993).
- [82] H. Bartholin, J. Beille, D. Bloch, P. Boutron, and J. L. Féron, *J. Appl. Phys.* **42**, 1679 (1971).
- [83] L. Benito, J. I. Arnaudas, M. Ciria, C. de la Fuente, A. del Moral, R. C. C. Ward, and M. R. Wells, *Phys. Rev. B* **70**, 052403 (2004).
- [84] L. Benito, M. Ciria, C. de la Fuente, J. I. Arnaudas, R. C. C. Ward, and M. R. Wells, *Phys. Rev. Lett.* **94**, 227204 (2005).
- [85] E. R. Callen and H. B. Callen, *J. Phys. Chem. Solids* **16**, 310 (1960).
- [86] Per-Anker Lindgård, *Phys. Rev. Lett.* **36**, 385 (1976); J. Jensen, *ibid.* **37**, 951 (1976); Per-Anker Lindgård, *ibid.* **37**, 954 (1976).
- [87] T. Moriya, *Phys. Rev.* **120**, 91 (1960).
- [88] R. J. Elliott and M. F. Thorpe, *J. Appl. Phys.* **39**, 802 (1968).
- [89] J. Jensen, *Phys. B (Amsterdam)* **86–88**, 32 (1977).
- [90] J. S. Koubel and C. D. Graham, *J. Appl. Phys.* **28**, 340 (1957).
- [91] J. O. Artman, *IEEE Trans. Magn.* **21**, 1271 (1985).
- [92] J. J. Rhyne and A. E. Clark, *J. Appl. Phys.* **38**, 1379 (1967).
- [93] E. R. Callen and H. B. Callen, *J. Phys. Chem. Solids* **27**, 1271 (1966).
- [94] J. Duthie and V. Heine, *J. Phys. F: Met. Phys.* **9**, 1349 (1979).
- [95] J. J. Rhyne, Ph.D. thesis, Iowa State University, 1965.
- [96] K. Ha, M. Ciria, R. C. O'Handley, P. W. Stephens, and P. Pagola, *Phys. Rev. B* **60**, 13780 (1999).
- [97] J. H. Basson and C. A. B. Ball, *Phys. Status Solidi A* **46**, 707 (1978).
- [98] S. W. Sun and R. C. O'Handley, *Phys. Rev. Lett.* **66**, 2798 (1991); R. C. O'Handley and S. W. Sun, *J. Magn. Magn. Mater.* **104–107**, 1717 (1992).
- [99] A. del Moral, M. Ciria, J. I. Arnaudas, R. C. C. Ward, and M. R. Wells, *J. Appl. Phys.* **81**, 5311 (1997).
- [100] A. del Moral, M. Ciria, J. I. Arnaudas, M. R. Wells, R. C. C. Ward, and C. de la Fuente, *J. Phys.: Condens. Matter* **10**, L139 (1998).
- [101] D. Sander, *Rep. Prog. Phys.* **62**, 809 (1999).
- [102] A. del Moral, M. Ciria, J. I. Arnaudas, and C. de la Fuente, *Phys. Rev. B* **57**, R9471 (1998).
- [103] K. Starke, F. Heigl, A. Vollmer, M. Weiss, G. Reichardt, and G. Kaindl, *Phys. Rev. Lett.* **86**, 3415 (2001).
- [104] G. Song, A. Remhof, K. Theis-Bröhl, and H. Zabel, *Phys. Rev. Lett.* **79**, 5062 (1997).
- [105] M. Lucht, M. Lerche, H.-C. Wille, Yu. V. Shvyd'ko, H. D. Rüter, E. Gerdau, and P. Becker, *J. Appl. Crystallogr.* **36**, 1075 (2003).
- [106] L. Benito, J. I. Arnaudas, C. de la Fuente, A. del Moral, P. A. J. de Groot, M. R. Wells, and R. C. C. Ward, *J. Magn. Magn. Mater.* **272–276**, 2058 (2004).
- [107] E. Callen, *J. Appl. Phys.* **53**, 8139 (1982).
- [108] J. Mayer, C. P. Flynn, and M. Rühle, *Ultramicroscopy* **33**, 51 (1990); G. Gutekunst, J. Mayer, and M. Rühle, *Philos. Mag. A* **75**, 1329 (1997).
- [109] P. M. Reimer, H. Zabel, C. P. Flynn, and J. A. Dura, *Phys. Rev. B* **45**, 11426 (1992).
- [110] A. Gibaud, R. A. Cowley, D. F. McMorrow, R. C. C. Ward, and M. R. Wells, *Phys. Rev. B* **48**, 14463 (1993).
- [111] H. Li, D. Tian, J. Quinn, Y. S. Li, S. C. Wu, and F. Jona, *Phys. Rev. B* **45**, 3853 (1992).
- [112] J. H. van der Merwe, *Philos. Mag. A* **45**, 145 (1982); E. Bauer, *Appl. Surf. Sci.* **11–12**, 479 (1982).
- [113] J. Narayan, P. Tiwari, X. Chen, J. Singh, R. Chowdhury, and T. Zheleva, *Appl. Phys. Lett.* **61**, 1290 (1992).
- [114] J. Narayan and B. C. Larson, *J. Appl. Phys.* **93**, 278 (2003).
- [115] R. Perez-Casero, J. Perrière, A. Gutierrez-Llorente, D. Defourneau, E. Millon, W. Seiler, and L. Soriano, *Phys. Rev. B* **75**, 165317 (2007).
- [116] G. R. Trichy, D. Chakraborti, J. Narayan, and J. T. Prater, *Appl. Phys. Lett.* **92**, 102504 (2008).
- [117] F. J. Darnell, *Phys. Rev.* **130**, 1825 (1963).